

3-D climate simulations for the detectability of Proxima Centauri b

DANIELE GALUZZO,¹ CHIARA CAGNAZZO,² FRANCESCO BERRILLI,¹ FEDERICO FIERLI,³ AND LUCA GIOVANNELLI¹

¹*Department of Physics, University of Rome Tor Vergata, Via della Ricerca Scientifica, 1, I-00133, Rome, Italy*

²*Institute of Marine Sciences (ISMAR), National Research Council (CNR), Via del Fosso del Cavaliere, 100, I-00133, Rome, Italy*

³*Institute of Atmospheric and Climate Sciences (ISAC), National Research Council (CNR), Via del Fosso del Cavaliere, 100, I-00133, Rome, Italy*

(Received April 16, 2019; Accepted January 15, 2021)

Submitted to ApJ

ABSTRACT

The discovery of a planet orbiting around Proxima Centauri, the closest star to the Sun, opens new avenues for the remote observations of the atmosphere and surface of an exoplanet, Proxima b. To date, three-dimensional (3D) General Circulation Models (GCMs) are the best available tools to investigate the properties of the exo-atmospheres, waiting for the next generation of space and ground-based telescopes. In this work, we use the PlanetSimulator (PlaSim), an intermediate complexity 3D GCM, a flexible and fast model, suited to handle all the orbital and physical parameters of a planet and to study the dynamics of its atmosphere. Assuming an Earth-like atmosphere and a 1:1 spin/orbit configuration (tidal locking), our simulations of Proxima b are consistent with a day-side open ocean planet with a superrotating atmosphere. Moreover, because of the limited representation of the radiative transfer in PlaSim, we compute the spectrum of the exoplanet with an offline Radiative Transfer Code with a spectral resolution of 1 nm. This spectrum is used to derive the thermal phase curves for different orbital inclination angles. In combination with instrumental detection sensitivities, the different thermal phase curves are used to evaluate observation conditions at ground level (e.g., ELT) or in space (e.g., JWST). We estimated the exposure time to detect Proxima b (assuming an Earth-like atmosphere) thermal phase curve in the FIR with JWST with signal-to-noise ratio $\simeq 1$. Under the hypothesis of total noise dominated by shot noise, neglecting other possible extra contribution producing a noise floor, the exposure time is equal to 5 hours for each orbital epoch.

Keywords: planets and satellites: atmospheres — planets and satellites: terrestrial planets — stars: individual (Proxima Centauri) — techniques: photometric

1. INTRODUCTION

A planet in the habitable zone of Proxima Centauri was detected in [Anglada-Escudé et al. \(2016\)](#) and confirmed recently in [Damasso et al. \(2020\)](#) and [Suárez Mascareño et al. \(2020\)](#). The planet, known as Proxima b, has not been observed as a transiting planet ([Davenport et al. 2016](#); [Kipping et al. 2017](#); [Liu et al. 2018](#); [Blank et al. 2018](#); [Feliz et al. 2019](#); [Jenkins et al. 2019](#)) and the estimated geometric probability of a transit is about 1.5%, ([Anglada-Escudé et al. 2016](#)). As a

consequence, constraints can exclusively be set on the orbit semi-major axis and on the planet's revolution period, leaving mass, radius, and density of the planet to be assumed.

Such an indeterminacy on the physical parameters as well as on the chemical composition of a possible atmosphere or ocean/land distribution, makes every hypothesis on the climate of Proxima b extremely speculative. Nevertheless, thanks to the proximity of Proxima b, remote observations of its atmosphere and its surface will be possible in the next decade (see e.g. [Kuhn et al. 2018](#)).

Nevertheless, some authors started assessing the Proxima b observation feasibility with current or forthcoming telescopes, investigating the possible detection limits.

Turbet et al. (2016) used a 3D General Circulation Model (GCM), derived from LMDZ (Hourdin et al. 2006) and assuming an Earth-like atmosphere to compute synthetic emission spectra of the planet, proposed for the first time to observe Proxima b with the James Webb Space Telescope (JWST), either with direct imaging or with thermal phase curves. Kreidberg & Loeb (2016), using an analytic *toy climate model* to presume the planet thermal phase curve, estimated in more details the JWST noise, and how the infrared thermal phase curve could be used to reveal the presence of an atmosphere on Proxima b. Lovis et al. (2017) proposed a theoretical setup in which Proxima b could be observed with a 8-m class telescope through a high resolution high contrast technique. Results similar to Turbet et al. (2016) were obtained by Boutle et al. (2017) using the Met Office Unified Model (Walters et al. 2017), which has a higher spectral resolution than LMDZ. In this work, we propose a new set-up of simulations for the Proxima b atmosphere performed with an intermediate complexity, flexible and fast 3D GCM model integrated with an offline 1D Radiative Transfer Code (RTC). Specifically, the 3D GCM is a modified version of the Planet Simulator (PlaSim, Fraedrich et al. 2005a) developed at University of Hamburg and based on the Reading multi-level spectral Simple Global Circulation Model (SGCM) described by Hoskins & Simmons (1975). This model, developed to maximize the compatibility with the comprehensive European Centre Hamburg (ECHAM) GCM, has been applied and tested in different research fields, including: climate change and variability studies (Lunkeit et al. 1998, Bordi et al. 2007 and Bordi et al. 2015), atmospheric dynamics and thermodynamics theoretical studies (Pérez-Muñuzuri et al. 2005, Seiffert et al. 2007, Kunz et al. 2009, Schmittner et al. 2011, Bordi et al. 2012a and Fraedrich 2012), sensitivities studies for Earth climate (Fraedrich et al. 2005b, Romanova et al. 2006, Lucarini et al. 2010a, Bordi et al. 2012b, Bathiany et al. 2012 and Knietzsch et al. 2015), simulations of Solar System planetary atmosphere (Grieger et al. 2004, Segschneider et al. 2005 and Stenzel et al. 2007) and simulations of planetary atmosphere in general (Lucarini et al. 2010b, Lucarini et al. 2013, Pascale et al. 2013, Boschi et al. 2013, Linsenmeier et al. 2015, Gómez-Leal et al. 2018 and Gómez-Leal et al. 2019). PlaSim is a fast and flexible model, adaptable to extensively alter planetary parameters, but, at the same time, it takes into account as many processes occurring on Earth’s atmosphere as possible. However, PlaSim only provides the integrated planetary atmosphere radiation within three bands, two

for the shortwave radiation and one for the longwave radiation. Thus, to explore the planet emission spectra and to derive thermal phase curves, we combine the RTC *uvspec* to PlaSim. *uvspec* is included in the libRadTran library (Emde et al. 2016) and uses the *DIScrete Ordinate Radiative Transfer* (DISORT) solver, reviewed by Stamnes et al. (1988) and Tsay et al. (2000). In this work, *uvspec* is used in an offline configuration, i.e. it is not directly implemented within the PlaSim code, but it runs on PlaSim outputs: the atmospheric state (e.g. trace gas profiles, temperature and pressure profiles, surface properties and eventually cloud liquid water content, cloud droplet size) obtained by the PlaSim 3D simulation is given as input to *uvspec* for each atmospheric vertical column. Our approach, in particular the offline radiative transfer calculations, provides robust results which are in line with those obtained with more complex models. Furthermore, libRadTran model allows us to have an accurate representation of the atmospheric emission spectra, useful to estimate the signal-to-noise ratio and evaluate the detection limits of broadband planetary emission for different orbital configurations.

This article is structured as follows. In Section 2 we present the known properties and parameters of the Proxima system. In Section 3 we describe the interactions between PlaSim and *uvspec* and we discuss the assumptions and parameterizations used in our simulation. In Section 4 the dynamical properties of an Earth-like atmosphere for Proxima b are reported, assuming its minimum mass as the planet mass. In Section 5, we evaluate the importance of planetary atmosphere and climate when assessing the observational limits through the use of thermal phase curves technique. Finally, in Section 6 we report our conclusions.

2. INPUTS FOR THE SIMULATION OF PROXIMA CENTAURI SYSTEM

2.1. *Proxima Centauri stellar spectral irradiance*

Proxima Centauri is the Solar System nearest star with a distance of 4.244 ± 0.001 light-years (Gaia Collaboration et al. 2018). It is a red dwarf of spectral type M5.5e (Bessell 1991), with estimated radius and mass $R_{\star} = 0.141 \pm 0.021 R_{\odot}$ and $M_{\star} = 0.120 \pm 0.015 M_{\odot}$ (Anglada-Escudé et al. 2016), respectively. The effective temperature estimated by Ribas et al. (2017) is $T_{\star}^{eff} = 2980 \pm 80$ K. Proxima Centauri peak of emission is in the Near-Infrared region and the spectral energy distribution is largely different from a G-type, Sun-like star. A comparison between Sun and Proxima Centauri spectral energy distributions is shown in Figure 1, where the star fluxes are evaluated at the

top-of-the-atmosphere (TOA) of Earth and the planet Proxima b, respectively.

Proxima Centauri spectrum is obtained following Meadows et al. 2018 and using the version 2.2 of the MUSCLES Treasury Survey data products, discussed in France et al. (2016), Youngblood et al. (2016) and Loyd et al. (2016). The total irradiance of Proxima Centauri used in this work, which was obtained by integrating the red curve in Figure 1, is equal to $885 \pm 44 \text{ W m}^{-2}$. This value is similar to that of Boutle et al. (2017) and Del Genio et al. (2019), equal to 881.7 W m^{-2} , while it turns out to be about 8% less than the irradiance proposed by Turbet et al. (2016), as already discussed by Boutle et al. (2017). Recently, observations of Proxima b compatible with super-flare occurrence, probably produced by magneto-convective processes similar to those observed on a small scale in our sun, have been reported (Howard et al. 2018). We know that in the solar case the magnetic activity of the star causes variations in irradiance. Small variations ($\simeq 0.1\%$) are reported in the case of total solar irradiance (i.e. bolometric irradiance), but these can lead to considerable variations ($\simeq 10 - 100\%$) in particular spectral ranges, for example in the EUV or UV (e.g. Criscuoli 2019).

We therefore expect that Proxima b also has a variable luminosity, both bolometric and spectral. However, Jenkins et al. (2019) reported Spitzer Space Telescope observations of Proxima Centauri that showed reduced stellar activity at near-to-mid infrared spectral range with respect to the optical one. In this paper, for simplicity, we will assume a constant star luminosity, i.e., a constant stellar spectral flux.

The presence of planetary atmospheres results from complex mechanisms involving stellar wind, flares, Coronal Mass Ejections, and the presence of a planetary magnetic field or other shielding effects. Zuluaga et al. (2013) suggested that Proxima b may have a planetary magnetic field if the planet has an Earth-like interior. The expected high dynamic pressure of Proxima Centauri wind pose hard constraints on the possibility for Proxima b to host an atmosphere on Gyr timescale. Nevertheless, the presence of a magnetosphere can help to conserve an exoplanet's atmosphere by reducing the erosion effects from stellar winds (e.g. See et al. 2014; Dong et al. 2017). Furthermore, the atmospheric escape rate crucially depends on many parameters (e.g. stellar wind properties, composition and thickness of the atmosphere). Here, we assume an Earth-like atmosphere with oxyc composition.

2.2. Proxima b planetary parameters

Proxima Centauri b, has been detected using the radial velocity method. The measured revolution period is 11.186 Earth days, with the orbit semi-major axis equal to 0.0485 AU. Because of the proximity to the host star, the planet should be captured in a 3:2 or 1:1 spin-orbit resonance, depending on the orbit eccentricity e , as described by Ribas et al. (2016). A threshold value of $e < 0.35$ was set from the observations by Anglada-Escudé et al. (2016). In this work, we consider a planet captured in synchronous rotation (tidal locking) on a circular orbit ($e = 0$) with an obliquity (axial tilt) equal to zero. Such configuration causes the planet to have a permanent day-side and night-side, with a fixed sub-stellar point which always receives the same amount of stellar radiation. The principal physical and orbital parameters used in this work for Proxima b are summarized in Table 1. They indicate the exact values introduced in our models and, for this reason, the relative uncertainties of these parameters are not reported in this table. In order to establish radius (r_p) and gravity acceleration (g_p) at the surface, we assume that the planet, for the edge-on orbital configuration, has a spherical shape with the same mean density of the Earth. The radius corresponding to the minimum mass is $r_p = 1.08 R_\oplus$. In Section 4 we present a detailed climatological analysis for the edge-on configuration, thus assuming the planet minimum mass ($1.27 M_\oplus$) as its mass. However, we perform several climate simulations with adjusted radius and mass values to correctly estimate the thermal phase curve of Proxima b. For smaller values of the orbital plane inclination angle ι , the planet increases in mass, and thus in radius. This has a significant effect on both the emission and reflected spectra of the planet. In particular, consequences on reflected light were extensively studied by Kane et al. (2017). To estimate the mass and radius changes for different orbital plane inclinations, we assume a simple mass-radius relation (see Swift et al. 2012; Kane & Gelino 2012; Kane et al. 2017), and in particular the one assumed by Turbet et al. (2016) for Proxima b, $r_p \propto (M/\sin \iota)^{0.27}$. Although orbit inclination, true mass and radius are unknown, the planet has $\sim 84\%$ probability to be in the terrestrial regime (Kane et al. 2017). In particular, a density transition and a planet composition dominated by volatile materials in non-terrestrial regime can be expected for a mass $> 5.1 M_\oplus$, corresponding to an orbit inclination $\iota < 15^\circ$ (Kane et al. 2017). Thus, we exclude the range $\iota < 15^\circ$ from our analysis. Furthermore, the recent discovery of Proxima c (Damasso et al. 2020) may help in further constraining Proxima b planetary parameters. Kervella et al. (2020) combine spectroscopic orbital pa-

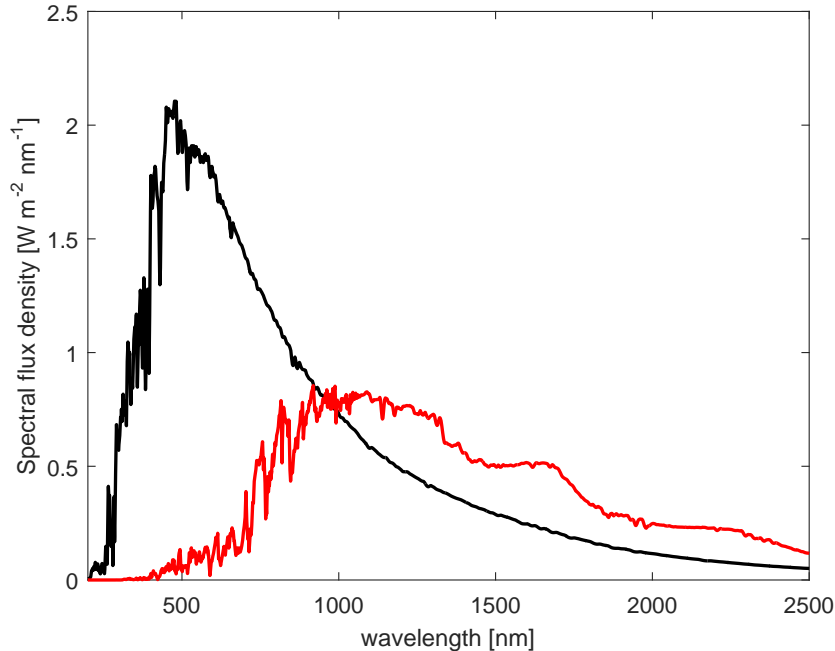


Figure 1. Sun (black curve, <http://kurucz.harvard.edu/>) and Proxima Centauri (red curve, [Meadows et al. 2018](#)) spectral irradiances as measured and evaluated at the top of the atmosphere of Earth and Proxima b, respectively.

rameters from HARPS and UVES with the astrometric proper motion anomaly (PMa) from HIPPARCOS and Gaia DR2, constraining Proxima c orbital inclination to two symmetric possible values, having the same $\sin i$: 152 ± 14 deg for a prograde orbit ($90^\circ \leq i \leq 180^\circ$) and 28 ± 14 deg for a retrograde orbit ($0^\circ \leq i \leq 90^\circ$). Assuming the coplanarity of the orbits of the two planets, the mass of Proxima b is then $2.1_{-0.6}^{+1.9} M_\oplus$, likely posing the planet in the terrestrial regime.

3. PLASIM AND LIBRADTRAN SETTINGS

PlaSim is a model derived from the Earth System Models (ESM) and its default configuration is set to reproduce the Earth climate. Consequently, the implemented parameterizations for the radiative transfer calculation within the atmosphere are based on the incoming solar radiation, and, in particular, on the Total Solar Irradiance (TSI) value, which is $\simeq 1361 \text{ W m}^{-2}$ (e.g. [Kopp 2018](#)). Nonetheless, in order to study the atmosphere of Proxima b taking into account the different spectral energy distribution of Proxima Centauri, the parameterizations have to be modified. In particular, the stellar contribution in PlaSim simulations is parameterized by three quantities defined at the planet TOA: the total stellar irradiance S_0 in W m^{-2} , the normalized fraction of S_0 in the ultraviolet and visible (UV-VIS) spectral region, E_1 , and the normalized fraction of S_0 in the near infrared (NIR) spectral region, E_2 . These two spectral regions are considered in our model as the

shortwave radiation. Although the output quantity provided by PlaSim are the integrated flux along all the shortwave range, the calculations in the source code are performed considering the separation between the two mentioned broadbands and the physical processes occurring within each one of them. Specifically: in the UV-VIS band, defined for wavelengths $\lambda < 0.75 \mu\text{m}$, pure cloud scattering, ozone absorption and Rayleigh scattering are taken into account without water vapor absorption, whereas in the NIR band, defined for wavelengths $\lambda > 0.75 \mu\text{m}$, cloud scattering and absorption and water vapor absorption are considered. Following this parameterization with a given stellar spectral irradiance $I(\lambda, T)$ in $\text{W m}^{-2} \text{ nm}^{-1}$, the resulting total irradiance in W m^{-2} can be obtained as

$$S_0 = \int_0^\infty I(\lambda, T) d\lambda, \quad (1)$$

and consequently, the normalized energy flux fractions in the two spectral regions described above can be computed as

$$E_1 = \frac{\int_0^{\lambda_\tau} I(\lambda, T) d\lambda}{S_0}, \quad (2)$$

and

$$E_2 = 1 - E_1, \quad (3)$$

where $\lambda_\tau = 0.75 \mu\text{m}$.

The normalized flux fractions derived from the Proxima Centauri spectrum in Figure 1 are $E_1 = 0.23$, and

Table 1. Proxima b Keplerian and planetary parameters assumed in PlaSim simulations.

Proxima Centauri b: derived and assumed quantities.		
Parameter	Symbol	Value
Orbital period	P	11.186 Earth days [†]
Orbit eccentricity	e_p	0.0 [‡]
Orbit semi-major axis	a	0.0485 AU [†]
Obliquity	α	0.0 deg [‡]
Minimum mass	M_{min}	1.27 M_{\oplus} [†]
Mean density	$\rho_p = \rho_{\oplus}$	5514.0 kg m ⁻³ [‡]
Radius	r_p	1.08 R_{\oplus} [‡]
Surface gravitational acceleration	g_p	10.6 m s ⁻² [‡]
Rotation rate	ω_p	6.5×10^{-6} rad s ⁻¹ [‡]

NOTE—[†] Measured or derived value by [Anglada-Escudé et al. \(2016\)](#); [‡] Assumed value for the simulation. Radius and surface gravitational acceleration refer to the edge-on configuration.

$E_2 = 0.77$, respectively and are modified in the PlaSim source code accordingly.

The longwave radiation parameterization in PlaSim includes CO₂, ozone, water vapor and clouds. The scheme uses one only spectral band, with broadband emissivity and transmissivity calculations based on [Manabe & Möller \(1961\)](#) and [Sasamori \(1968\)](#) for a clear sky atmosphere and vertical discretization based on [Chou et al. \(2002\)](#). This means that, as well as in the shortwave case, the radiation emitted by the planet is given as an integrated quantity along all the longwave spectral range, also known as the outgoing longwave radiation (OLR, [Petty 2006](#)).

Since our aim is to study Earth-like planets, we use a simple approach and we assume an Earth-like atmosphere. The initial surface pressure is assumed equal to 1000 hPa. Moreover, an ozone layer is maintained with a prescribed vertical profile parameterized by [Green \(1964\)](#), in order to reproduce the Earth’s one, with the exception that, because of the completely different insolation pattern between Proxima b and the Earth, we neglect the typical ozone seasonality, keeping its vertical and meridional distribution constant over time. For an active star, as Proxima Centauri is, the impact of the stellar UV variation on the ozone vertical distribution should be considered. Due to surface magnetic structures, the stellar UV variability can be described by [FUV-MUV] color index variation during the activity cycle (e.g., [Lovric et al. 2017](#), [Criscuoli et al. 2018](#), [Berrilli et al. 2020](#)). However, for simplicity, in this work we hypothesize a constant stellar flux (i.e. no stellar variability), postponing to a future work a detailed study of the connection between stellar UV activity and

planetary ozone distribution.

Of importance, due to its spectral properties, the albedo of sea-ice is significantly reduced around an M star with respect to a G star like the Sun ([Joshi & Haberle 2012](#); [Shields et al. 2013](#); [Turbet et al. 2016](#); [Boutle et al. 2017](#); [Del Genio et al. 2019](#) among others). In order to take this into account, in PlaSim the maximum value of broad band albedo over sea ice has been set to 0.27, based on the calculation of [Turbet et al. \(2016\)](#). In the PlaSIM code, the sea ice albedo parameterization depends on the temperature, following the formula: $R_S = \min(R_S^{max}, 0.5 + 0.025(273. - T_i))$. Where T_i is the temperature over sea-ice and the prescribed maximum sea ice background albedo R_S^{max} , originally set to a default value of 0.7 for the Earth, has been set to 0.27 in this study.

The carbon dioxide concentration is maintained fixed to 360 ppm during the simulation. This is chosen in order to compare our results with the works of [Turbet et al. \(2016\)](#), [Boutle et al. \(2017\)](#) and [Del Genio et al. \(2019\)](#) in which similar parameters were used. Water vapor concentration is directly computed by PlaSim in a specific module, using pressure and temperature fields in order to determine its properties for each time-step.

The planet is initialized as an aquaplanet, i.e. a planet with a surface entirely covered by an ocean. This choice is motivated by two considerations. Firstly, [Tian & Ida 2015](#) showed that, in the habitable zones around M dwarfs, there are two favored types of planets with Earth-like mass which are aquaplanet and desert planets with orders of magnitude less surface water than on Earth. Secondly, land mass distribution alters both dynamics and thermodynamics in different ways depend-

ing on the orography and the surface properties, such as albedo and soil type. Since any land mass distribution introduced in the model would be completely arbitrary, the most straightforward choice is to totally neglect land masses. Furthermore, although [Del Genio et al. \(2019\)](#) showed that ocean dynamics could play a relevant role on tidally-locked planet climate, in this work we simulate a thermodynamic slab ocean of 50 meters depth, where the horizontal and vertical mixing are neglected. The advantage of using a slab ocean instead of a full ocean (i.e. an ocean for which the 3D Navier-Stokes equations are numerically solved as well as for the atmosphere) is that it allows the climatic system to reach a steady state in less than a few decades, returning a fast numerical simulation which enables sensitivity evaluation to parameter variations.

In order to obtain the effect of the synchronous rotation of the planet, we modify the PlaSim radiation module source code, to fix the position of the star in the planet sky at each simulation timestep. We run the Proxima b climate equilibrium simulation for a period of 110 Earth years with a temporal resolution of 45 minutes, that is the default timestep of the model. The output temporal resolution is 1 Earth day. Because of the spurious variability of the system introduced by the initial non-equilibrium spin-up of the simulation, a specific period at the beginning of the simulation is discarded. This is chosen following the stabilization of the surface temperature variability, i.e. when no long-term trends are found, and the mean surface temperature reach a steady state. We find that this system stabilization occurs after 10 years from the beginning of the simulation. Model outputs are gridded on a 128×64 longitude-latitude grid, with 20 vertical pressure levels, from 1000 hPa to 50 hPa, setting the sub-stellar point above the equator, at 180° E of longitude.

As discussed above, PlaSim returns integrated fluxes in both shortwave and longwave spectral ranges. However, integrated fluxes are not sufficient for our purposes. Given that our aim is to determine whether Proxima b can be detected by analyzing its thermal emission within specific bands from current or future telescopes observations, we evaluate the planet thermal infrared emission in narrower spectral bands compared to PlaSim outputs. In order to perform the radiative transfer calculation on the atmosphere of Proxima b, obtaining high resolution synthetic emission spectrum, we use the *uvspec* model and the DISORT method. In particular, given the spectrally resolved stellar irradiance at planet TOA and the vertical profiles of the planetary atmosphere constituents, DISORT solves the 1D plane-parallel radiative transfer equation, returning radiances, irradiances, and

actinic fluxes¹ as outputs. In this work, we use the spectral irradiance of Proxima Centauri shown in Figure 1 as stellar input for DISORT, whereas atmospheric vertical profiles are extracted from PlaSim simulation, considering the atmospheric columns above each grid-box. We indicate these columns as *grid-columns*. Specifically, the extracted profiles within a grid-column are: *i*) atmospheric pressure, *ii*) temperature, *iii*) air density, *iv*) ozone, *v*) water vapor concentration and *vi*) carbon dioxide concentration. Furthermore, our implementation takes into account the cloud properties such as the liquid water content, the cloud droplet effective radius and the total optical depth. The output from *uvspec* are then used to estimate the line-by-line emission spectra of the simulated planetary atmosphere, with a spectral resolution of 1 nm, for each time-step and each grid-column from which we reconstruct thermal emission from planet TOA. Because of the imposed planetary axial and orbital symmetry, the year-to-year variability of the different atmospheric constituents (including water vapour and clouds), estimated as the standard deviation of the yearly time series over 100 Earth years, in the three regions is very small, as shown in Figure 2 for the temperature profile only. This small atmospheric variability allows us to assume stationary vertical profiles. This means that we can use the mean vertical profiles within each grid-column, as representative for the entire period of simulation.

4. PROXIMA CENTAURI B CLIMATE

4.1. *Thermodynamic properties of Proxima b atmosphere*

The planet surface temperature is largely used as a climatological proxy to estimate the habitability conditions on a planet ([Kasting et al. 1993](#)) or to study the fluctuations between different multiple steady states of its climate ([Lucarini et al. 2013](#)). Using the planetary parameters and atmospheric composition discussed in Section 2.2, the resulting mean surface temperature field from our PlaSim simulation shows an insolation-symmetric pattern with temperatures below the water freezing temperature T_{ice} on the night-side of the planet surface, and an open ocean on most of the day-side. Surface maximum temperature is located to the east of the sub-stellar point. This is likely due to the superrotating atmosphere and will be discussed in more details later in this section. Surface temperature ranges from a min-

¹ The actinic flux is the radiant quantity used to calculate different photodissociation rates. It represents the total number of photons, or radiation, incident at a point ([Madronich 1987](#)).

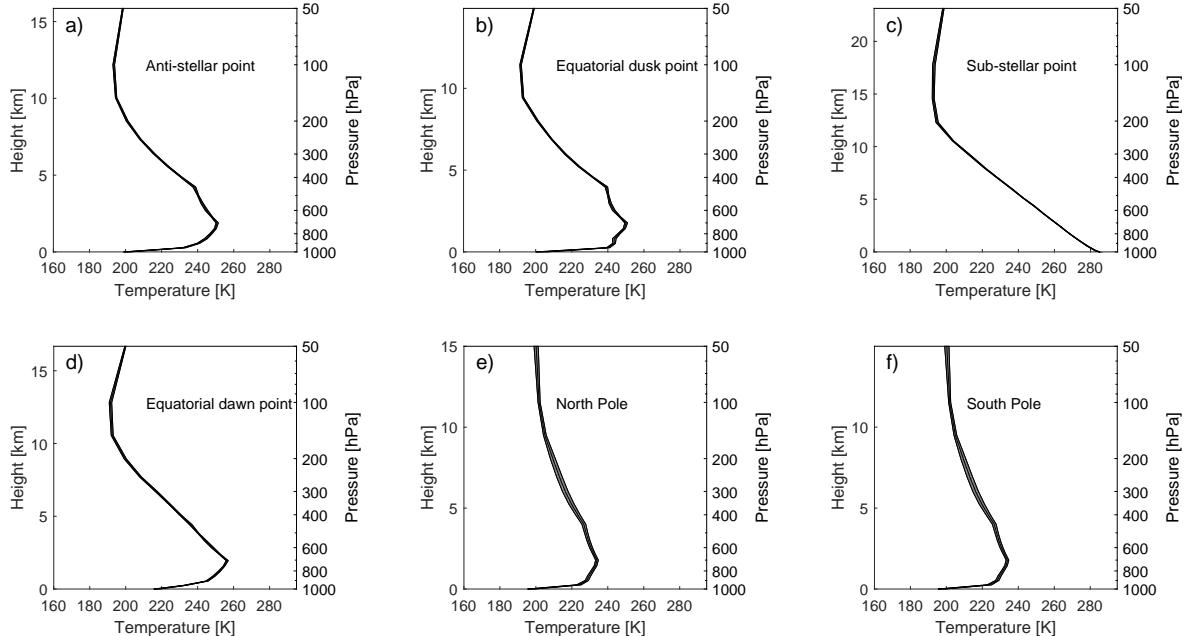


Figure 2. Temperature mean vertical profiles (black curve) and relative $\pm 1\sigma$ deviation from mean profile (gray-shaded area) for six grid-column of PlaSim simulation, relative to different regions of Proxima b: *a*) anti-stellar point; *b*) equator dusk point; *c*) sub-stellar point; *d*) equator dawn point; *e*) North Pole; *f*) South Pole. On the x -axis the value of temperature is reported, while on two y -axis the height and isobar level are reported, respectively. The different height of planet TOA in sub-stellar region, depends on planet thermal structure. The 1σ deviation is evaluated on the entire period of simulation (100 Earth years) and the relative maximum deviation for each panel is: *a*) ± 0.78 K at surface; *b*) ± 1.32 K at surface, *c*) ± 0.36 K at 11.5 km; *d*) ± 0.60 K at surface; *e*) ± 0.88 K at surface; *f*) ± 0.87 K at surface.

imum value of 160 K to a maximum value of 295 K. These values are smaller compared to those reported by Turbet et al. (2016) for similar simulation settings, that were 200 K and 300 K, respectively, but comparable to those shown by Boutle et al. (2017). Moreover, our surface temperature maximum on the day-side is comparable with that found by Del Genio et al. (2019), whereas surface temperature minimum is about 20 K higher. Furthermore, our results regarding the planet surface region where $T > T_{ice}$ are in line with that obtained by all the three aforementioned studies for similar simulation settings. Given the comparable results obtained using either intermediate complexity models (PlaSim in our study) or the more sophisticated GCMs (as reported in previous literature), such simplified models may represent an innovative and promising tool for future climate studies, especially to simulate future exoplanetary observations.

Thermodynamic processes determine the amount of infrared radiation emitted by the planet towards space and consequently they can be used to set observational limits. One of the main absorbers in an Earth-like atmosphere is water, both as vapor and liquid (i.e. in the clouds). In our simulation, the atmospheric liquid

water content in clouds (w_L) is lower than Earth, with a maximum of $1.73 \times 10^{-4} \text{ kg m}^{-3}$ located in the first layer above the planet surface in the day-side and with a dry night-side. For reference, the maximum value of cloud liquid water content on Earth has been evaluated by Hu et al. (2007) to be around $5.0 \times 10^{-4} \text{ kg m}^{-3}$.

4.2. Atmospheric dynamics

The planetary surface temperature pattern reported in Figure 3, causes a convective structure in the day-side which brings the surface air masses to ascend up to 15 km. This convective flow is consistent with the planet’s mean global circulation shown in Figure 4. In this figure, the mass stream function ψ is superimposed to the zonally averaged zonal wind. ψ is defined as in Ceppi & Hartmann (2013):

$$\psi = -\frac{2\pi r_p}{g_p} \int_0^p [\bar{v}] \cos \theta dp' \quad (4)$$

where g_p is the gravitational acceleration, $[\bar{v}]$ is the zonal mean of the meridional wind, θ is the latitude and p is the pressure level. The mass stream function indicates the meridional flows on Proxima b and the formation

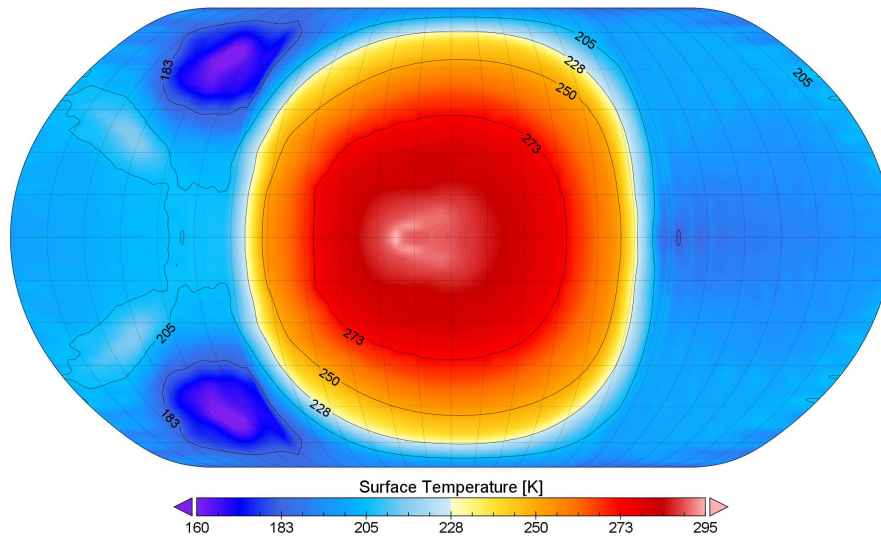


Figure 3. Mean surface temperature. The tidal-locking of the planet produces the symmetrical pattern of Proxima Centauri b surface temperature: higher temperatures in the region of the sub-stellar point, with the presence of an open ocean ($T_{ice} = 273.15K$) and colder temperatures in the night-side of the planet. Planet rotation is assumed clockwise in the simulation. This map is shown as it would be for a planet with anticlockwise (prograde) rotation, for easy comparison with previous works. See e.g. the position of the cold points in Fig.2 of [Boutle et al. 2017](#) and Fig. 6 of [Turbet et al. 2016](#).

of a Hadley cell-like circulation which surrounds the entire planet from equator to poles. The cell presents a clockwise branch in the northern hemisphere (solid lines in Figure 4) and an anticlockwise counterpart, in the southern hemisphere (dashed lines in Figure 4). This global circulation is in agreement with results from similar studies reported in the literature (e.g., [Turbet et al. 2016](#); [Boutle et al. 2017](#); [Komacek & Abbot 2019](#)) for a planet rotation period of the order of one tenth of the Earth’s one.

This implies that the planetary atmosphere dynamics, triggered by the constant insolation on the day-side, is driven by the interaction of the meridional circulation with the Coriolis force due to the planet rotation. This results in an equatorial symmetric jet stream at 300 hPa (Figure 4).

Furthermore, this tidally-locked rocky planet, exhibits a superrotating atmosphere. This result is comparable to previous results (e.g., [Joshi et al. 1997](#), [Heng & Vogt 2011](#), [Edson et al. 2011](#), [Wordsworth et al. 2011](#) [Showman et al. 2013](#), [Merlis et al. 2013](#)). Superrotation is a condition whereby the atmospheric axial angular momentum is locally greater than the surface axial angular momentum. The specific equatorial angular momentum of the planet is $M_0 = \omega r_p^2$ and it only depends on the planet radius and rotation rate, whereas the atmosphere’s axial angular momentum M_a also depends

on the zonal wind and it can be expressed as

$$M_a = r_p \cos \theta (\omega r_p \cos \theta + u), \quad (5)$$

where θ is the latitude.

Assuming that the atmospheric angular momentum is equal to the planet equatorial angular momentum,

$$M_a = M_0, \quad (6)$$

a zonal wind threshold value can be derived as a function of θ :

$$u_m = \frac{\omega r_p \sin \theta^2}{\cos \theta}. \quad (7)$$

Hence, u_m represents the threshold value for which the atmosphere would be co-rotating with the planet surface at the equator. In Figure 5 the threshold value u_m and zonal mean zonal wind at different pressure levels for Proxima b are shown for global, night-side and day-side averages. The equatorial superrotation condition is satisfied in the region between 30° S – 30° N with the exception of the first atmospheric layer which represents the planet surface. Such an exception seems to suggest that the aforementioned surface displacement of the warm region from the sub-stellar point is not due to superrotation. However, this result is biased by the fact that the zonal mean of zonal wind is evaluated by global averages. Nevertheless, when performing the same analysis considering the night-side and the day-side separately, the superrotation condition is satisfied also at

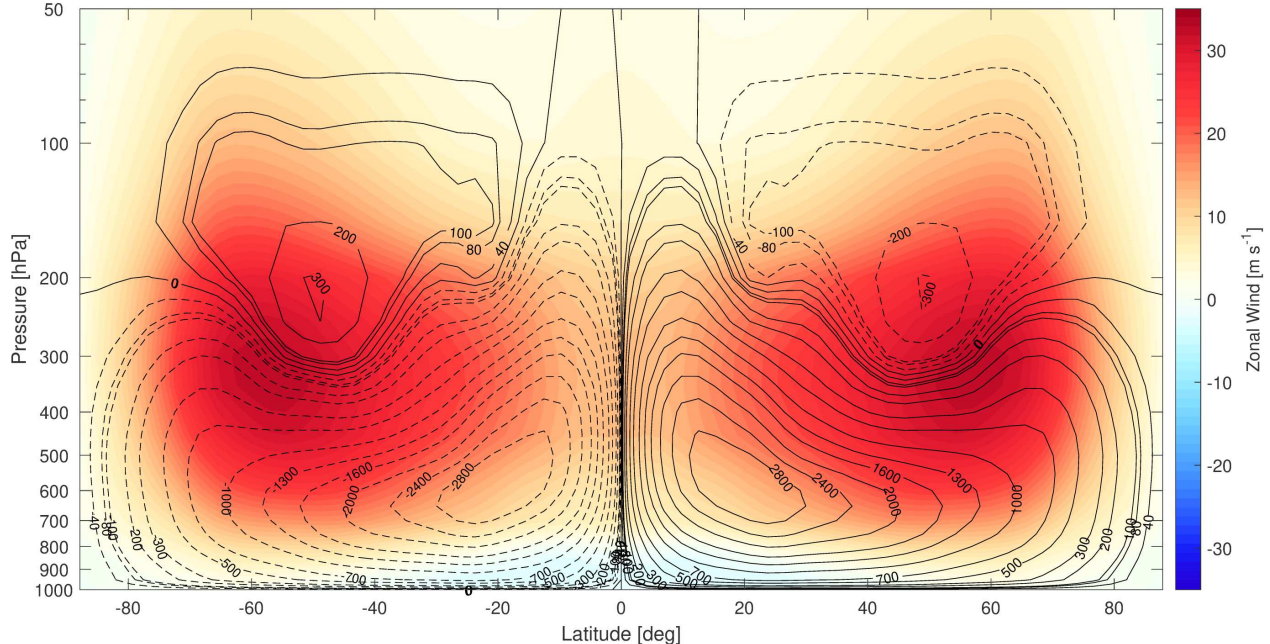


Figure 4. Zonally averaged zonal wind (colored contours) and mass stream function (black contour lines). Hadley cell-like structure in the atmosphere of Proxima Centauri b, driven by the constant insolation in the day-side. Colors represent the zonal mean of the zonal wind, where positive values are for easterlies winds (from west to the east) and negative values are for westerlies winds (from east to the west). The black lines show the mass stream function: the solid lines denote clockwise circulation ($\psi > 0$), while the dotted lines denote anticlockwise circulation ($\psi < 0$). The numbers upon the lines are the relative values of ψ in 10^6 kg s^{-1} units. The mass stream function gives the extent of the Hadley cell-like circulation which, in the case of Proxima Centauri b, extends horizontally from the equator to poles, and vertically above 150 hPa.

the planet surface, but only in day-side, as shown in Figure 5c and discussed by Showman & Guillot (2002) and Showman & Polvani (2011). This result suggests that the east shift in surface temperature maximum is indeed due to the superrotating atmosphere. This also clearly demonstrates that, in case of tidally-locked planets, the average evaluations over the entire planet surface could lead to substantial misinterpretations of key climatic features and thus we strongly support the analysis of both hemispheres, separately. Moreover, the advantage of using 3D over 1D or 2D models is evident. In fact, these latter models cannot simulate the full dynamical structure of an atmosphere, which is only possible in 3D models.

5. DETECTABILITY OF PLANETARY ATMOSPHERE EMISSIONS FROM SPACE AND GROUND-BASED OBSERVATIONS

Proxima b has not yet been observed with direct imaging. This is due to the angular separation of 37 milliarcseconds between the planet and the host star (Anglada-Escudé et al. 2016) and the planet-to-star contrast in different spectral regions. Lovis et al. (2017) explored the possibility to observe Proxima b in the

visible coupling SPHERE and ESPRESSO at VLT, to reach a contrast of 10^{-7} . Turbet et al. (2016) showed the opportunity to exploit higher planet-to-star contrast (10^{-5}) at $10 \mu\text{m}$ using JWST as well as the advantages that will be offered by ELT at $1 \mu\text{m}$ with a contrast (10^{-7}) using high-resolution spectroscopy. Observations in the thermal IR wavelengths provide distinctive information to constrain planet atmospheric properties. However, given that the spatial resolution depends on wavelength in diffraction limited instruments, the IR direct imaging is limited to exoplanets with larger semi-major axis respect to the same technique applied in the optical spectral region. ELT will provide a significant improvement, nevertheless, due to its diffraction limit, direct imaging for Proxima b, even for a 39 m aperture, is limited in wavelength up to $3 \mu\text{m}$ (Turbet et al. 2016). Thus, a possible strategy to overcome this limitation is to characterize the planet’s atmosphere and climate studying the thermal phase curve (e.g. Selsis et al. 2011, Cowan et al. 2012 and Maurin et al. 2012). We use PlaSim and the offline RTC to identify the spectral regions more sensitive to contrast variations during the orbital period. We evaluate this effect firstly for the OLR, applying the *uvspec* model to PlaSim out-

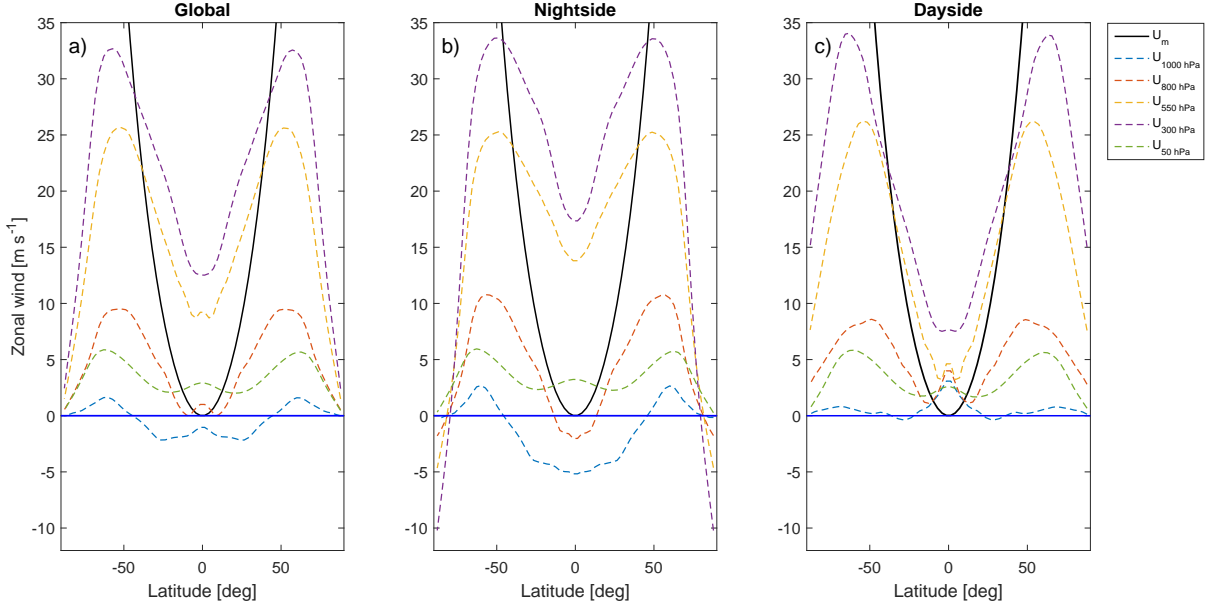


Figure 5. Atmospheric superrotation. Angular momentum conserving wind u_m (black curve) and zonal mean zonal wind (colored dashed lines) as a function of latitude θ (x -axis), for planet a) global mean, b) night-side mean and c) day-side mean. Each zonal mean wind curve represents the x component of the wind (y -axis) at different pressure levels, namely 1000 hPa (blue-dashed curve), 800 hPa (red-dashed curve), 550 hPa (yellow-dashed curve), 300 hPa (purple-dashed curve) and 50 hPa (green-dashed curve). The blue horizontal line represents the zero mean of the zonal wind. If a colored curve is above the solid black curve for a given latitude range, the condition $u > u_m$ is satisfied, and the relative atmospheric layer is in an equatorial superrotation state in that latitude range.

puts. Typically, the peak of emission of an Earth-like planet in the habitable zone is expected to be in the mid-IR region around $10\text{-}20\ \mu\text{m}$. Hence, we investigate the thermal phase curves in specific spectral bands, using [Boutle et al. 2017](#) approach, to evaluate the planet detectability with space or ground-based instruments.

5.1. Planetary spectra and thermal phase curves

To evaluate spectral properties of the planetary atmosphere, we follow the method described in Section 3. Planetary spectral thermal fluxes at the TOA for different planet regions, are shown in Figure 6. Because of the synchronous rotation, the planet thermal flux has a strong dependence from longitude and latitude, with the peak of emission at $\lambda \approx 14\ \mu\text{m}$. The *uvspec* module applied to the PlaSim outputs returns 8192 thermal spectra, one for each latitude/longitude grid-column of the simulation (i.e. 64×128 spectra). In Figure 6, only four of these spectra are shown as reference: the thermal spectra as seen from the planet TOA above the substellar and anti-stellar points and above the warm and cold points. The carbon dioxide absorption/emission feature can be seen at $\lambda \approx 15\ \mu\text{m}$ (i.e. $\tilde{\nu} \approx 600\ \text{cm}^{-1}$) in all panels and it is clear how its emission temperature remains the same in each region, being $\sim 200\ \text{K}$. In particular, on the planet night-side, the carbon diox-

ide signature is clearly visible being the feature with the maximum peak of emission.

The planet emission spectra is used to derive the thermal phase curve. The expected flux from Proxima b is obtained integrating the thermal emission over the whole surface of the planet taking into account the distance and the position angle. Since the exact geometry of the planet-star system is not currently known we consider several possible inclinations of the orbital plane with respect to an observer on Earth. For this purpose, we use the visibility function

$$V(\theta, \phi, t, \theta_0) = \max\{\sin(\theta) \sin(\theta_0) \cos[\phi - \phi_0(t)] + \cos(\theta) \cos(\theta_0), 0\} \quad (8)$$

described by [Cowan et al. \(2013\)](#), to obtain the visible region of the planet as a function of the orbital parameters at given orbital time. The visibility function V , depends on 4 parameters: *i*) the planet longitude $\phi \in (0, 2\pi]$; *ii*) the planet co-latitude $\theta \in (0, \pi)$; *iii*) the sub-observer longitude $\phi_0 \in (0, 2\pi]$; and *iv*) the sub-observer co-latitude $\theta_0 \in (0, \pi)$.

The sub-observer longitude is a function of the orbital time t and it can be linked to the phase angle ξ (see Figure 8a), via the relationship $\xi = \Omega t$, where Ω is the

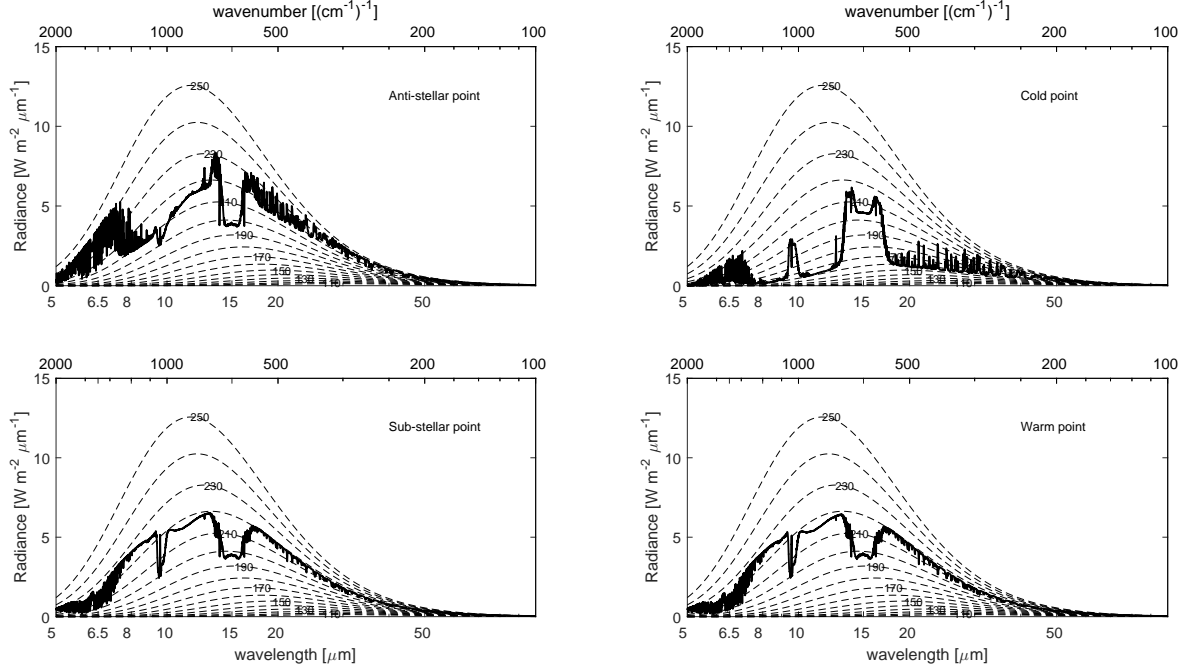


Figure 6. Infrared emission spectra. Infrared emission spectra at Proxima b TOA, as a function of wavelength λ (bottom x-axis) and wavenumber $\tilde{\nu}$ (top x-axis) are obtained with *uvspec*, above different regions of the planet: a) the anti-stellar point (0°N , 0°E); b) the cold point (66°N , 290°E); c) the sub-stellar point (0°N , 180°E) and d) the warm point (1°N , 199°E). Dashed lines represent the ideal black body emission from Planck’s law curves relative to the black body temperatures from 100 K to 300 K, with 10 K separation. The radiative effect of the atmospheric component can be seen on the curves and in particular, the carbon dioxide signature, around $\lambda = 15 \mu\text{m}$ ($\tilde{\nu} = 666 \text{ cm}^{-1}$), the ozone signature, around $\lambda = 9.6 \mu\text{m}$ ($\tilde{\nu} = 1040 \text{ cm}^{-1}$) and the water vapor signatures at $\lambda < 7 \mu\text{m}$ ($\tilde{\nu} > 1300 \text{ cm}^{-1}$).

planet orbital angular velocity (i.e. the revolution rate). Since we assumed a tidally-locked planet, the revolution period is equal to the rotation period and $\Omega = \omega$. The sub-observer co-latitude instead, corresponds to the planet orbital plane inclination ι , with respect to the observer.

Finally, by performing the substitution $\theta_0 \rightarrow \iota$, the planet thermal emission $F_p(\xi, \iota)$ is given by:

$$F_p(\xi, \iota) = \int_0^{2\pi} \int_0^\pi I(\theta, \phi) V(\theta, \phi, \xi, \iota) d\theta d\phi, \quad (9)$$

where $I(\theta, \phi)$ is the planet integrated thermal flux in a selected spectral range $\lambda_1 \leq \lambda \leq \lambda_2$, for each latitude/longitude box of the simulation.

The integrated flux from Proxima Centauri, F_\star , is considered constant with time for any wavelength range. This means that we are neglecting any possible influence of the stellar variability. We define the planet/star contrast $\Phi(\xi, \iota)$:

$$\Phi(\xi, \iota) = \frac{F_p(\xi, \iota)}{F_\star}, \quad (10)$$

where F_p is the planet atmospheric emission. Both F_p and F_\star are evaluated in the same spectral range. In

particular, we are interested in the amplitude $A(\iota)$ of the planet thermal phase curve defined as

$$A(\iota) \equiv \Phi_{max}(\xi, \iota) - \Phi_{min}(\xi, \iota), \quad (11)$$

since the amplitude modulation of the phase curve is the measurable quantity for unresolved exoplanetary systems. Furthermore, $A(\iota)$ must be compared to the achievable photometric precision, which crucially depends on the photons available in the considered spectral range. The ratio between these two quantities identifies the most suitable band for the observations.

In Figure 8b, the planet thermal phase curve computed in the OLR spectral range ($3 \mu\text{m} \leq \lambda \leq 100 \mu\text{m}$) is shown for different orbital plane inclinations.

Although we evaluated the thermal phase curves for several inclination angles $0^\circ \leq \iota \leq 180^\circ$, here we show only the results obtained for $\iota \leq 90^\circ$, because the system symmetry produces completely specular curves for $\iota > 90^\circ$. The presence of atmosphere and its role in heat advection produces a not perfectly symmetric phase curve.

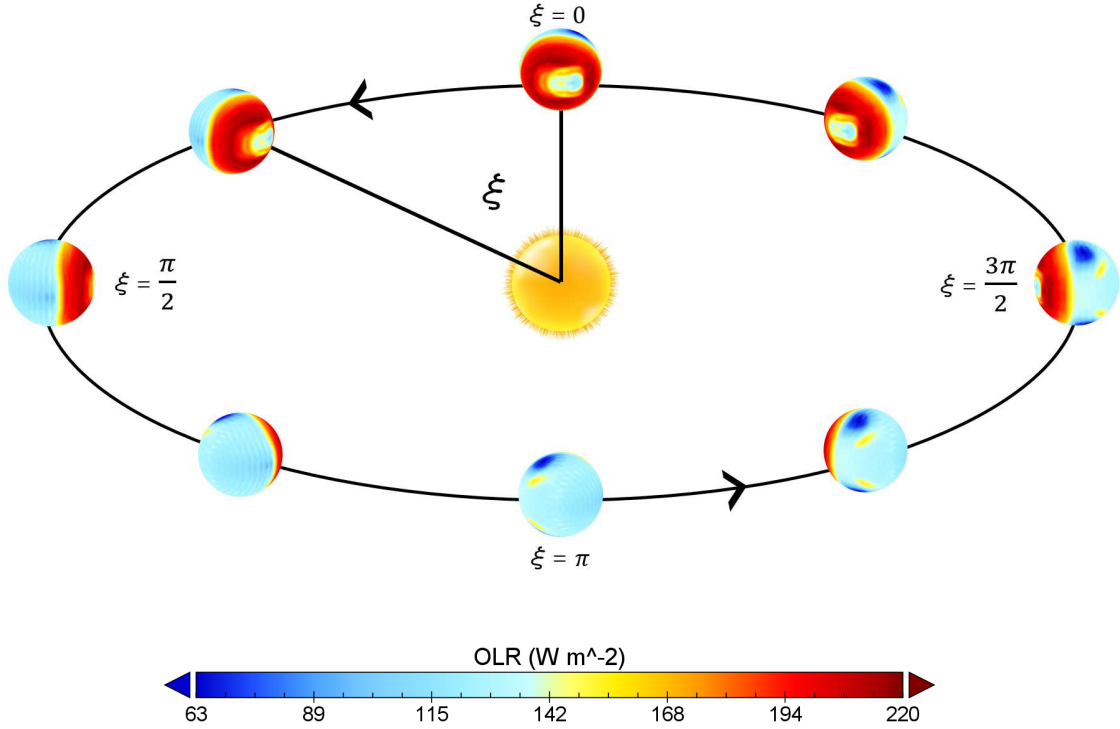


Figure 7. Proxima b orbit. The figure represents Proxima b on its circular orbit around the host star. Because of the 1:1 spin/orbit resonance, an outside observer can explore all sides of the planet in a single revolution. Surface color represents the amount of OLR emission: red regions represent the emission maximum, whereas the dark blue regions represent the emission minimum.

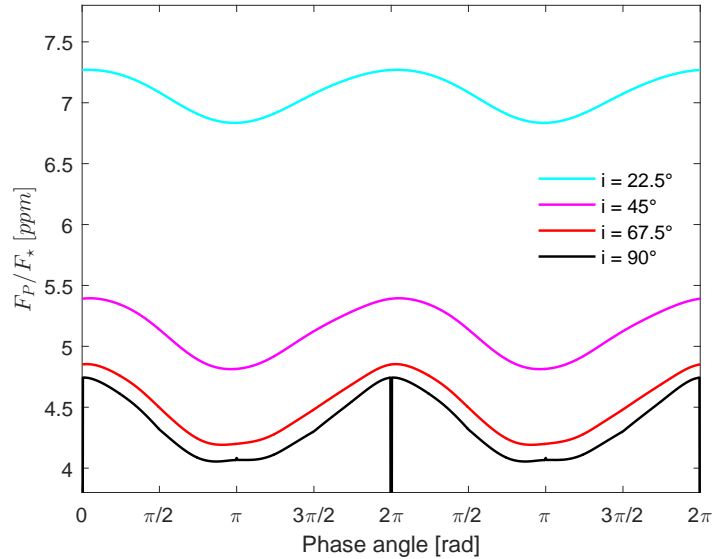


Figure 8. Planet phase curves. Planet/Star contrast in the OLR region ($3 \mu\text{m} \leq \lambda \leq 100 \mu\text{m}$), during two complete orbits of Proxima b around the host star. Each curve represents a different inclination angle of the planet orbital plane with respect to the observer. The black curve represents the thermal emission for an edge-on geometry, i.e. the case of a transiting planet. For this reason, the value of $\Phi(\xi, 90)$ drops to zero at $\xi = 2\pi$ (secondary eclipse). Also, the small effect due to primary eclipse is visible at $\xi = \pi$.

5.2. Proxima b detectability from space observatories

Future detection of Proxima b thermal emission is evaluated considering the technical specification of the James Webb Space Telescope (JWST), specifically the case of the imaging mode of the Mid-Infrared Instrument (MIRI, Wells et al. 2015). The photometric bands of the MIRI imager (MIRIM, Bouchet et al. 2015) are considered and we compute the amplitude of the phase curve, fixing the orbital inclination angle to 90° . Given the Proxima Centauri spectrum, the photometric precision achievable in each band is also computed, expressed in terms of the minimum detectable amplitude $A_0^{(N)}$. This is calculated assuming photon noise limited observations and it will be extensively described later in this section. In Table 2 these quantities are compared and the ratio between the two amplitudes is found to be maximum in the MIRI F2100W passband filter, corresponding to the spectral band $18.5 \mu\text{m} \leq \lambda \leq 23.5 \mu\text{m}$.

In Table 3 the maximum values of $\Phi(\xi, \iota)$, Φ_{max} and the relative amplitude A , evaluated in the above mentioned spectral band, are reported as a function of the system inclination. The geometric probability of transit for Proxima b is very small ($\sim 1.5\%$, Anglada-Escudé et al. 2016) and recent Spitzer Space Telescope observations ruled out planetary transits at the 200 ppm level at $4.5 \mu\text{m}$ (Jenkins et al. 2019). Thus, the effect of a transit is excluded from subsequent analysis. The $\iota = 90^\circ$ case has to be intended as an almost edge-on configuration with no-transit. The amplitude A is expected to decrease with inclination, considering that day-side becomes partially visible along the full orbit. Nevertheless, this decrease is compensated by the increase of the planet mass and, in turns, its radius (Turbet et al. 2016). The amplitude A results in this case almost constant with respect to the orbital inclination. Our results are also in line with Kane et al. (2017) results regarding the planet/star contrast.

In order to derive the detectability limits of Proxima b using the JWST, the signal-to-noise ratio on the MIRIM detector is computed for the passband filter F2100W. Assuming a photon noise limited observation, two different methods are used to evaluate the photometric precision. In both cases we consider an exposure time $\tau = 5$ hours, which is a small fraction of the planet orbital period ($\tau^* < P/50$). The observing strategy simulated with the JWST Exposure Time Calculator (ETC)² consists of several short exposures (~ 1.2 s) to avoid detector saturation. The ETC simulation was set to use the SUB128 subarray of the MIRI detector in fast mode.

Proxima Centauri is a bright source, so an individual exposure of 1.2 s almost exploits the full dynamic range of the camera, thus the readout noise is not a limiting factor for the observations. The readout time for the SUB128 subarray is 0.119 s, therefore the duty cycle is $\sim 90\%$ and 5.5 hours are needed for a 5 hours exposure time.

Our first method consists in computing the number of photons, within the assigned spectral band, collected by the instrument, as per Yang et al. (2013):

$$N = \varepsilon \frac{\pi \mathcal{A}_T^2}{4} \tau \left(\frac{R_\star}{D} \right)^2 \int_{\lambda_1}^{\lambda_2} \frac{F_\star(\lambda)}{E(\lambda)} d\lambda, \quad (12)$$

where \mathcal{A}_T is the telescope collecting area, τ is the exposure time, R_\star is the star radius, D is the star-observer distance, $F_\star(\lambda)$ is the stellar spectral energy distribution and $E = hc/\lambda$ is the energy of a photon for a given wavelength λ . In the case of JWST, the primary mirror effective collecting area is $\mathcal{A}_T = 25 \text{ m}^2$ (Gardner et al. 2006). Furthermore, we also consider the factor ε in order to take the MIRIM filter efficiency into account, which is 25% for the F2100W filter³.

The instrument photometric precision is estimated considering a photon shot noise limited observation, obtaining $PP_N = 5.2$ ppm. The corresponding minimum detectable amplitude of the phase curve at $1\text{-}\sigma$ level is equal to twice the computed photometric precision: $A_0^{(N)} = 10.3$ ppm. In Figure 9a, the gray-shaded bands have an amplitude equal to the computed $A_0^{(N)}$.

The second method we use to evaluate the photometric precision of JWST exploits the ETC. The JWST ETC estimates the infrared background using a model including many celestial sources, *e.g.*, zodiacal light, interstellar medium, and cosmic infrared background (Reach et al. 1997; Kelsall et al. 1998; Krick et al. 2012), in addition to telescope thermal and scattered light. Moreover, it achieves accurate calculation of signal-to-noise ratio, considering the MIRIM instrumental characteristics and the filter response functions. Using JWST ETC, we obtain a photometric precision $PP_{ETC} = 7.8$ ppm, and a corresponding $A_0^{(ETC)} = 15.6$ ppm (see Figure 9b). This means that the photometric performance evaluated with the ETC, is lower but comparable with the one obtained using the method of Yang et al. (2013).

In Figure 10 we combine the instrumental photometric performance and the planet thermal phase curve amplitude together in order to derive the lower limit of the exposure time given a certain planet orbital plane

² <https://jwst.etc.stsci.edu/>

³ <https://jwst-docs.stsci.edu/display/JTI/MIRI+Filters+and+Dispersers>

Table 2. Amplitude of the phase curve $A(90^\circ)$, minimum detectable amplitude $A_0^{(N)}$ (24 hours integration time) and ratio between them for the photometric bands of JWST/MIRIM.

MIRIM filter	$A(90^\circ)$ (ppm)	$A_0^{(N)}$ (ppm)	$A(90^\circ)/A_0^{(N)}$
F560W	0.06	1.6	0.04
F770W	2.4	1.7	1.4
F1000W	8.3	2.4	3.5
F1130W	15.0	5.2	2.9
F1280W	13.6	3.4	4.0
F1500W	4.0	3.8	1.1
F1800W	24.7	4.9	5.0
F2100W	34.3	4.7	7.3
F2550W	14.0	9.9	1.4

Table 3. Planet/star thermal emission maximum contrast Φ_{max} and amplitude A for different orbital inclination angle ι (MIRI imager F2100W).

ι	Φ_{max} (ppm)	A (ppm)
22.5°	364	21.1
45°	271	23.4
67.5°	245	32.7
90°	240	34.3

inclination angle. In particular, we compare $A_0^{(N)}$ as a function of τ and A as a function of ι . A semi-empirical equation for $A(\iota)$ is obtained by fitting with a cubic function the four points resulting from our simulation and reported in Table 3. From this figure, we can also establish for which exposure time the instrumental photometric precision $A_0^{(N)}$ is sufficient for the detection of signature of the planet of amplitude $A(\iota^*)$, given its dependency on the inclination. For instance, in the case shown in Figure 10a, an exposure time of ~ 5 hours is necessary to detect planet thermal emission for all considered inclinations. We recall that, assuming coplanarity of Proxima b and Proxima c as in Kervella et al. 2020, it is possible to constrain the orbital plane inclination angle between 14° and 42° . The amplitude of the phase curve for those inclination is expected to be between ~ 15 ppm and ~ 30 ppm in the band $18.5 \div 23.5 \mu\text{m}$.

5.3. Proxima b detectability from ground-based observatories

In the previous section, the JWST photometric accuracy in the case of Proxima b observations has been computed. Such an approach can in principle be applied to similar observations performed from ground-based observatories. However, for ground-based infrared observations, mainly at mid-IR wavelengths (e.g. Berrilli et al. 1987, 1989, 1992), the background is large when compared to the emission of stellar sources. Further, this background emission is very sensitive to the telescope thermal and scattered light (at 10 microns the telescope emissivity can dominate over sky emission) and atmospheric status can fluctuate rather fast in time and in space.

Here, we compare estimated 1σ detection for both JWST-MIRIM and the mid-infrared imager and spectrograph METIS (Brandl et al. 2014) which will be installed at the Extremely Large Telescope (ELT) (Gilmozzi & Spyromilio 2007). ELT will be the largest

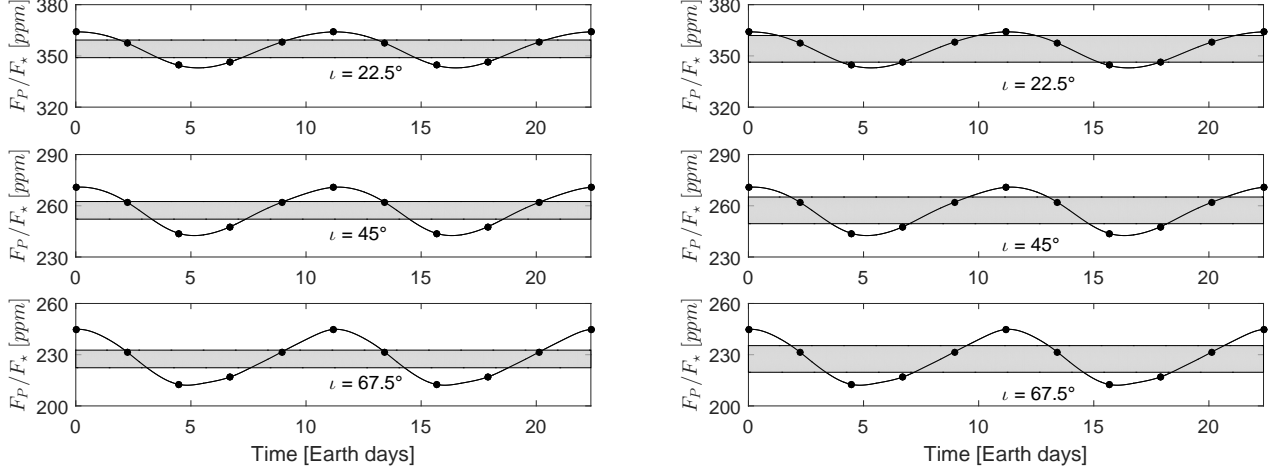


Figure 9. Five hours exposure time detection limits. The planet/star contrast (y-axis) in the spectral band $18.5 \div 23.5 \mu\text{m}$ as a function of time for a sample of three possible planet orbital plane inclination angles. Gray area represent the minimum detectable amplitude of the phase curve at $1\text{-}\sigma$ level for Proxima b (5 hours exposure time) obtained considering the photon number: a) derived from the stellar flux following Yang et al. (2013) (left) and b) the Exposure Time Calculator (ETC) of JWST, with MIRIM settings (right).

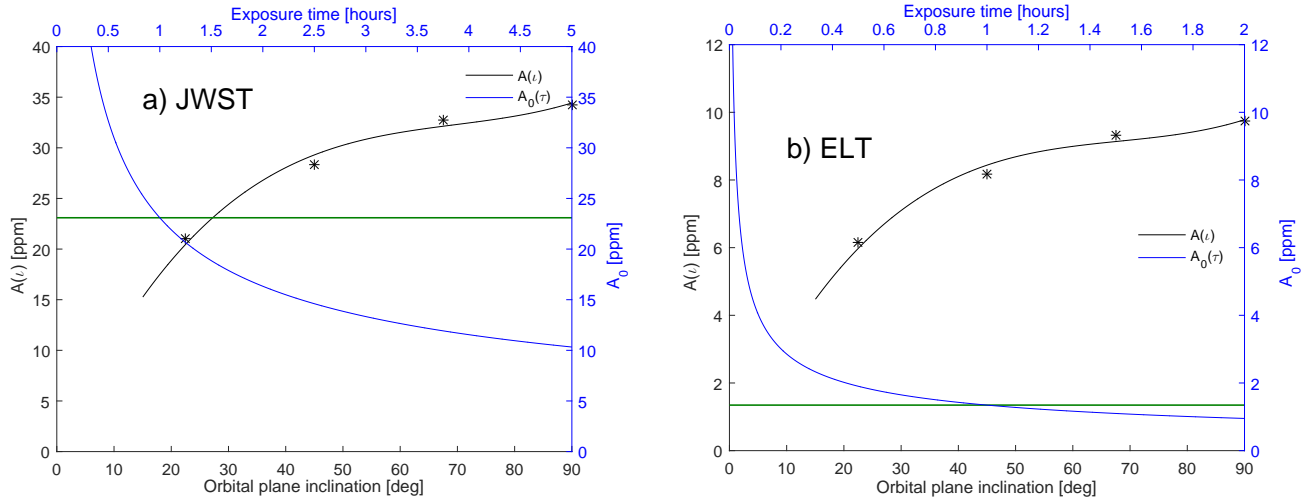


Figure 10. Proxima b atmosphere detection comparison. Comparison between JWST-MIRIM ($18.5 \div 23.5 \mu\text{m}$), panel a, and ELT-METIS ($8.3 \div 13.8 \mu\text{m}$), panel b, for 1σ detection of broadband Proxima b atmospheric emission. The black curves represent the semi-empirical thermal phase curve amplitude A as a function of the planet orbital plane inclination angle ι . Values of this function below $\iota = 15^\circ$ are not shown since they are outside the validity range of our model. Star symbols represent sample values of the amplitude A for the fixed inclination angles reported in Table 3. The blue curves represent the minimum detectable amplitude A_0 as a function of exposure time, evaluated as in Yang et al. (2013). The green horizontal line indicates the values of A_0 relative to an exposure time of 1 hour in both panels.

optical/NIR telescope in the world with a primary mirror of 39 meters diameter. The technical characteristics of the ELT METIS needed to perform our evaluation have been obtained from Brandl et al. (2014), Brandl et al. (2016), and Brandl et al. (2018). An attempt to estimate the performance of ELT METIS through a sensitivity model introducing a variety of sources is presented in Kendrew et al. (2010). However, in this work, we do not make assumptions about the

noise introduced by the instrument and the Earth atmosphere by limiting the analysis to only photometric shot noise. In order to estimate the photometric precision of METIS we assume a primary mirror collecting area for ELT $\mathcal{A}_{ELT} = 978 \text{ m}^2$ and a 10% efficiency.

The amplitude $A(\iota)$ is computed for the N band ($8.3 \div 13.8 \mu\text{m}$, see also Table 4) and it is shown as black star symbols in Figure 10. The values of $A(\iota)$ are smaller compared to those evaluated by JWST-MIRIM, this is

Table 4. Effective wavelengths, full width half maxima, zero-magnitude fluxes for the ESO infrared passbands used in this work, taken from [van der Bliek et al. 1996](#). We also report the corresponding amplitude of the phase curve $A(90^\circ)$, minimum detectable amplitude $A_0^{(N)}$ (1 hour integration time) and ratio between them for the same photometric bands.

Filter	λ_{eff}	FWHM	$F_\lambda(m_\lambda = 0)$	$A(90^\circ)$	$A_0^{(N)}$	$A(90^\circ)/A_0^{(N)}$
	μm	μm	$\text{Wm}^{-2}\text{nm}^{-1}$	ppm	ppm	
L'	3.771	0.580	5.58×10^{-14}	0.007	1.9	0.004
M	4.772	0.381	2.21×10^{-14}	0.065	2.3	0.03
N	11.055	5.47	$1,29 \times 10^{-15}$	9.7	1.7	16.5
Q_0	18.666	3.23	$1,09 \times 10^{-16}$	32.7	5.0	6.54

mainly due to the different spectral intervals used. Considering a 1 hour exposure time for ELT-METIS, a minimum detectable amplitude $A_0 = 1.7$ ppm is computed, which would be sufficient to detect planetary signature for all the range of considered orbital inclinations. Given the noise assumptions, the computed exposure time (1 hour) must be considered as a lower limit to achieve such a photometric precision. Given that the ELT aperture is considerably bigger compared to the JWST one and only considering photon shot noise, the ELT photometric precision in the N band is almost 14 times smaller than the JWST in the F2100W band.

Finally, a general method to detect and characterize exoplanets using the information coming from different IR bands is introduced. For this reason, the variation in time of the color of exoplanetary systems are analyzed. Calculations are performed using the ESO IR photometric bands, indicated by the letters **M**, **N** and **Q₀**, to maximize the planet contribution. These bands, with the relative zeropoint magnitude fluxes, are described in [van der Bliek et al. \(1996\)](#) and summarized in Table 4. We compute the color indices **M**–**N** and **N**–**Q₀** for the Proxima system as a function of the planet phase angle. We define the color variation as

$$\Delta(X - Y) = (X - Y) - \overline{(X - Y)}, \quad (13)$$

where X and Y are respectively **M** and **N** or **N** and **Q₀** and $\overline{(X - Y)}$ is the mean value over the orbital period. In Figure 11, we evaluate the color index variation for four different Proxima b orbital plane inclinations. If the planet had a face-on orbit inclination, there would be no color index variation, in contrast, approaching the edge-on inclination the color index variation increases. For Proxima Centauri System, the **M**–**N** and **N**–**Q₀** color variations are of the order of 8 ppm and 18 ppm, respectively, for an orbital plane inclination angle of 45° . Although these values are at the edge of the capabili-

ties of METIS, the color variation technique could open detection possibilities for the next generation ground-based large aperture telescopes.

6. CONCLUSIONS

In this work we propose and use a method to study the climate of a terrestrial exoplanet with an Earth-like atmosphere and we evaluate its detectability by photometry in the thermal IR bands. A fast and flexible 3D GCM (PlaSim) is used and modified in order to reproduce the atmosphere and the climate of the planet. Moreover, a robust RTC is run offline in order to determine the radiative properties of such an atmosphere. Intermediate complexity 3D GCMs have the potential to include more details compared to 1D atmospheric models, retaining enough computational speed to allow for parameter space exploration.

Our main conclusions are as follows:

1. *Proxima b climate simulation.* The recently discovered planet Proxima b is used as a case study, assuming a 1:1 gravitational resonance. A surface temperature distribution consistent with an open ocean day-side, and a cold and dry night-side is reported. This is in line with [Boutle et al. \(2017\)](#) and [Del Genio et al. \(2019\)](#). The permanent day-side heating is partially distributed in the night-side by the slow atmospheric circulation. Thus, in the night-side, energy is irradiated towards space in the form of IR radiation in a very efficient radiative cooling process. Consistent with other findings, e.g. [Selsis et al. \(2011\)](#), [Showman & Polvani \(2011\)](#), [Cowan et al. \(2012\)](#) and [Showman et al. \(2013\)](#), it has been found that the warmest place of the planet surface is not located at the sub-stellar point, but it stands eastwards to that region. This may be due to the atmospheric superrotation asso-

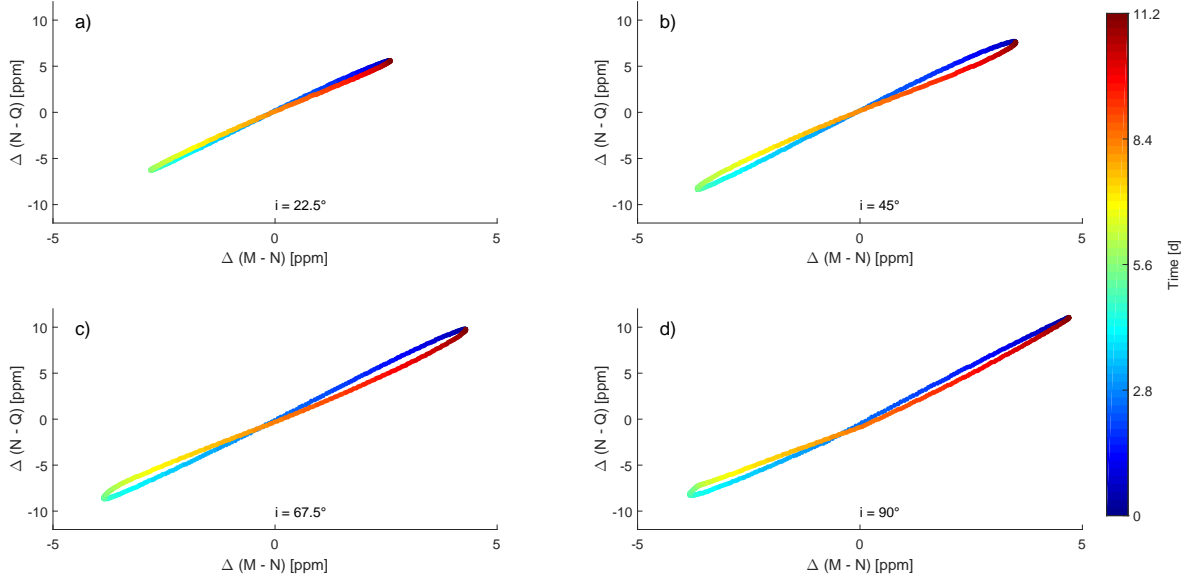


Figure 11. Color-color scatter plot. The color variation of the Proxima Centauri/Planet b system during one full orbit for four different orbital plane inclination angles, respectively 22.5° , 45° , 67.5° , and 90° . The color variation is obtained evaluating the magnitude of the system in three different bands reported in Table 4.

ciated with the planet rotation rate. The simulations presented here, performed with an intermediate complexity model integrated with an offline RTC, are in agreement with model runs made with more sophisticated GCMs on one hand and on the other hand they allow to compute the exoplanet spectrum with a resolution of 1 nm. Considering the very limited computational effort, intermediate complexity models with offline RTC represent a suitable tool to perform different sensitivity studies and, at the same time, to accurately estimate the emitted and reflected planet radiations.

2. *Detection via thermal phase curve.* Photometric measurements of the planet thermal emission with forthcoming instruments will be more easily exploited choosing the appropriate spectral band. This choice is not straightforward since, in each spectral band, it depends on the trade-off among the planet-to-star contrast, the amplitude of the thermal phase curve and the available photons, which affect the achievable photometric precision. In the case of cold planets, the contrast between the IR flux of the planet and that of the star is higher for $\lambda > 10 \mu\text{m}$. This is usually the spectral region where the amplitude of the thermal phase curve of a planet in the habitable zone is detectable with broad band photometry. However, as reported in the literature, the presence of

an atmosphere mitigates the amplitude of thermal phase curve given the role of circulation in heat redistribution (see Turbet et al. 2016; Boutle et al. 2017 for a more extensive description). This implies that, in similar conditions, the thermal phase curve modulation is smaller for a planet with atmosphere compared to a planet without it. Consequently, this affects the possible detection of such a planet, that is more favorable in case of the absence of an atmosphere. Therefore, a fast model to compute the emitted IR spectrum of an exoplanet, including the effects of its atmosphere, is needed to choose the most effective spectral band in thermal phase curve observations.

3. *Detection limits for JWST and ELT.* To understand the feasibility of a photometric detection of Proxima b, we evaluate the prospected limit of detection for the MIRIM instrument on board of the James Webb Space Telescope. Analyzing the infrared planet/star contrast for the F2100W filter of MIRIM ($\lambda = 21 \mu\text{m}$), we find that the amplitude of the planet thermal phase curve increases by more than one order of magnitude compared to the same parameter computed for the case of the OLR. Taking into account the collecting area of JWST, MIRIM filter efficiency and an exposure time of 5 hours, we evaluate a photometric precision of 5.2 ppm. We also computed the photometric precision using JWST Exposure Time Cal-

culator, obtaining, for the same exposure time, a photometric precision of 7.8 ppm. Our model predicts an amplitude of Proxima b thermal phase curve that is > 15 ppm all over the planet orbital plane inclination range $15^\circ > \iota > 90^\circ$, and therefore detectable at the level $S/N \simeq 1$ with the aforementioned photometric precision. By comparison, assuming photometric shot noise, a lower limit of ~ 1 hour is found for the exposure time needed for the detection in the case of ELT-METIS at $S/N \simeq 1$. In this case the N band is considered, where the achievable photometric precision is 0.85 ppm, and the amplitude of Proxima b thermal phase curve is > 4 ppm all over the planet orbital plane inclination range $15^\circ > \iota > 90^\circ$.

However, we have to note that in the case of JWST/MIRI this estimate is based on the assumption that total noise derives from shot noise, telescope thermal and scattered light, and from other celestial sources, *e.g.*, zodiacal light, interstellar medium, and cosmic infrared background (Reach et al. 1997; Kelsall et al. 1998; Krick et al. 2012) as computed using the JWST ETC. This estimate does not take into account any possible extra contribution that can potentially affect the noise floor. However the final performance of MIRI instrument will be fully evaluated only after the JWST commissioning, and this lead us to focus the analysis on photon-noise dominated observations. Nevertheless we briefly discuss here the expected performance of MIRI. Based on the performance of Spitzer, the noise floor for MIRI was estimated by Greene et al. (2016) to be ~ 50 ppm. Fauchez et al. (2019) revised the noise floor value to a more optimistic ~ 25 ppm at 1σ confidence level, that would allow a detection for an orbital plane inclination angle $\gtrsim 40$.

4. *Detection via color variations.* Finally, we consider an alternative method to detect exoplanets by analyzing the color variation of an exoplanetary system in the infrared bands due to the presence of an orbiting planet. Color variation is very sensitive to the orbital inclination and to the planet temperature gradient between day-side and

night-side. For a non-face-on orbit, the more the planet's hemispherical temperature difference is, the greater the color variation will be during the orbital period. For the case study of this work, the color index variation $\mathbf{M} - \mathbf{N}$ correlates with the variation $\mathbf{N} - \mathbf{Q}$. This correlation reflects the symmetry of the system under consideration. Such analyses can be very helpful to independently confirm the presence of non-transiting exoplanets analyzing the periodic color shift of a star.

To date, because of the lack of observations in the mid infrared region with sufficient photometric precision, characterization of the atmosphere of non-transiting terrestrial exoplanets is very challenging. To foster infrared broad band photometric observations of exoplanetary systems, an improvement in photometric precision (< 10 ppm), at wavelengths above the $10 \mu\text{m}$ is needed for the next generation telescopes. At the same time, the atmospheric models can pave the way for future measurement campaigns giving for instance the order of magnitude of the expected flux on telescopes, setting the observational limits and the required precision for the detection.

7. ACKNOWLEDGMENTS

This study was supported by grants from the Solar Physics and Space Physics group of the Department of Physics of the University of Rome Tor Vergata (<https://www.fisica.uniroma2.it/~solare>) and from the Atmospheric and Climate Sciences Institute (ISAC) of the Italian National Research Council (CNR) within the Joint Research PhD Program in Astronomy, Astrophysics and Space Science between the universities of Roma Tor Vergata, Roma Sapienza and INAF. We are also grateful to professors Nicolas Iro, Valerio Lucarini, Edilbert Kirk and Brunella Nisini for technical assistance and support. Thanks to Ilaria Giovannelli and Angela Stabile for proofreading the article. The authors thank the anonymous reviewer for her/his valuable help in improving the manuscript.

Software: PlaSim (Fraedrich et al. 2005a), libRadTran (Emde et al. 2016)

REFERENCES

- Anglada-Escudé, G., Amado, P. J., Barnes, J., et al. 2016, *Nature*, 536, doi: [10.1038/nature19106](https://doi.org/10.1038/nature19106)
- Bathiany, S., Claussen, M., & Fraedrich, K. 2012, *Climate Dynamics*, 38, 1775, doi: [10.1007/s00382-011-1037-x](https://doi.org/10.1007/s00382-011-1037-x)
- Berrilli, F., Ceccarelli, C., Liseau, R., et al. 1989, *MNRAS*, 237, 1, doi: [10.1093/mnras/237.1.1](https://doi.org/10.1093/mnras/237.1.1)
- Berrilli, F., Corciulo, G., Ingrassio, G., et al. 1992, *ApJ*, 398, 254, doi: [10.1086/171853](https://doi.org/10.1086/171853)

- Berrilli, F., Criscuoli, S., Penza, V., & Lovric, M. 2020, *SoPh*, 295, 38, doi: [10.1007/s11207-020-01603-5](https://doi.org/10.1007/s11207-020-01603-5)
- Berrilli, F., Lorenzetti, D., Saraceno, P., & Strafella, F. 1987, *MNRAS*, 228, 833, doi: [10.1093/mnras/228.4.833](https://doi.org/10.1093/mnras/228.4.833)
- Bessell, M. S. 1991, *AJ*, 101, 662, doi: [10.1086/115714](https://doi.org/10.1086/115714)
- Blank, D. L., Feliz, D., Collins, K. A., et al. 2018, *AJ*, 155, 228, doi: [10.3847/1538-3881/aabded](https://doi.org/10.3847/1538-3881/aabded)
- Bordi, I., Berrilli, F., & Pietropaolo, E. 2015, *Annales Geophysicae*, 33, 267, doi: [10.5194/angeo-33-267-2015](https://doi.org/10.5194/angeo-33-267-2015)
- Bordi, I., Fraedrich, K., Lunkeit, F., & Sutera, A. 2007, *Monthly Weather Review*, 135, 3118, doi: [10.1175/MWR3464.1](https://doi.org/10.1175/MWR3464.1)
- Bordi, I., Fraedrich, K., Sutera, A., & Zhu, X. 2012a, *Theoretical and applied climatology*, 109, 253
- . 2012b, *Theoretical and applied climatology*, 109, 245
- Boschi, R., Lucarini, V., & Pascale, S. 2013, *Icarus*, 226, 1724, doi: <https://doi.org/10.1016/j.icarus.2013.03.017>
- Bouchet, P., García-Marín, M., Lagage, P.-O., et al. 2015, *Publications of the Astronomical Society of the Pacific*, 127, 612, <http://stacks.iop.org/1538-3873/127/i=953/a=612>
- Boutle, I. A., Mayne, N. J., Drummond, B., et al. 2017, *Astronomy and Astrophysics*, 601, doi: [10.1051/0004-6361/201630020](https://doi.org/10.1051/0004-6361/201630020)
- Brandl, B. R., Feldt, M., Glasse, A., et al. 2014, in *Society of Photo-Optical Instrumentation Engineers (SPIE) Conference Series*, Vol. 9147, *Ground-based and Airborne Instrumentation for Astronomy V*, 914721, doi: [10.1117/12.2056468](https://doi.org/10.1117/12.2056468)
- Brandl, B. R., Agócs, T., Aitink-Kroes, G., et al. 2016, in *Society of Photo-Optical Instrumentation Engineers (SPIE) Conference Series*, Vol. 9908, *Ground-based and Airborne Instrumentation for Astronomy VI*, 990820, doi: [10.1117/12.2233974](https://doi.org/10.1117/12.2233974)
- Brandl, B. R., Absil, O., Agócs, T., et al. 2018, in *Society of Photo-Optical Instrumentation Engineers (SPIE) Conference Series*, Vol. 10702, *107021U*, doi: [10.1117/12.2311492](https://doi.org/10.1117/12.2311492)
- Ceppi, P., & Hartmann, D. L. 2013, *Journal of Climate*, 26, doi: [10.1175/JCLI-D-12-00414.1](https://doi.org/10.1175/JCLI-D-12-00414.1)
- Chou, M.-D., Suarez, M. J., & Liang, X. 2002, *Technical Report Series on Global Modeling and Data Assimilation*, 19
- Cowan, N. B., Fuentes, P. A., & Haggard, H. M. 2013, *Monthly Notices of the Royal Astronomical Society*, 434, 2465, doi: [10.1093/mnras/stt1191](https://doi.org/10.1093/mnras/stt1191)
- Cowan, N. B., Voigt, A., & Abbot, D. S. 2012, *The Astrophysical Journal*, 757, 80, <http://stacks.iop.org/0004-637X/757/i=1/a=80>
- Criscuoli, S. 2019, *ApJ*, 872, 52, doi: [10.3847/1538-4357/aaf6b7](https://doi.org/10.3847/1538-4357/aaf6b7)
- Criscuoli, S., Penza, V., Lovric, M., & Berrilli, F. 2018, *ApJ*, 865, 22, doi: [10.3847/1538-4357/aad809](https://doi.org/10.3847/1538-4357/aad809)
- Damasso, M., Del Sordo, F., Anglada-Escudé, G., et al. 2020, *Science Advances*, 6, eaax7467, doi: [10.1126/sciadv.aax7467](https://doi.org/10.1126/sciadv.aax7467)
- Davenport, J. R. A., Kipping, D. M., Sasselov, D., Matthews, J. M., & Cameron, C. 2016, *ApJL*, 829, L31, doi: [10.3847/2041-8205/829/2/L31](https://doi.org/10.3847/2041-8205/829/2/L31)
- Del Genio, A. D., Way, M. J., Amundsen, D. S., et al. 2019, *Astrobiology*, doi: [10.1089/ast.2017.1760](https://doi.org/10.1089/ast.2017.1760)
- Dong, C., Lingam, M., Ma, Y., & Cohen, O. 2017, *ApJL*, 837, L26, doi: [10.3847/2041-8213/aa6438](https://doi.org/10.3847/2041-8213/aa6438)
- Edson, A., Lee, S., Bannon, P., Kasting, J. F., & Pollard, D. 2011, *Icarus*, 212, doi: [10.1016/j.icarus.2010.11.023](https://doi.org/10.1016/j.icarus.2010.11.023)
- Emde, C., Buras-Schnell, R., Kylling, A., et al. 2016, *Geoscientific Model Development*, 9, doi: [10.5194/gmd-9-1647-2016](https://doi.org/10.5194/gmd-9-1647-2016)
- Faucher, T. J., Turbet, M., Villanueva, G. L., et al. 2019, *ApJ*, 887, 194, doi: [10.3847/1538-4357/ab5862](https://doi.org/10.3847/1538-4357/ab5862)
- Feliz, D. L., Blank, D. L., Collins, K. A., et al. 2019, *AJ*, 157, 226, doi: [10.3847/1538-3881/ab184f](https://doi.org/10.3847/1538-3881/ab184f)
- Fraedrich, K. 2012, *The European Physical Journal Plus*, 127, 53, doi: [10.1140/epjp/i2012-12053-7](https://doi.org/10.1140/epjp/i2012-12053-7)
- Fraedrich, K., Jansen, H., Kirk, E., Luksch, U., & Lunkeit, F. 2005a, *Meteorologische Zeitschrift*, 14, 299, doi: [doi:10.1127/0941-2948/2005/0043](https://doi.org/10.1127/0941-2948/2005/0043)
- Fraedrich, K., Jansen, H., Kirk, E., & Lunkeit, F. 2005b, *Meteorologische Zeitschrift*, 14, 305, doi: [10.1127/0941-2948/2005/0044](https://doi.org/10.1127/0941-2948/2005/0044)
- France, K., Loyd, P. R. O., Youngblood, A., et al. 2016, *ApJ*, 820, doi: [10.3847/0004-637X/820/2/89](https://doi.org/10.3847/0004-637X/820/2/89)
- Gaia Collaboration, Brown, A. G. A., Vallenari, A., et al. 2018, *A&A*, 616, A1, doi: [10.1051/0004-6361/201833051](https://doi.org/10.1051/0004-6361/201833051)
- Gardner, J. P., Mather, J. C., Clampin, M., et al. 2006, *Space Science Reviews*, 123, 485, doi: [10.1007/s11214-006-8315-7](https://doi.org/10.1007/s11214-006-8315-7)
- Gilmozzi, R., & Spyromilio, J. 2007, *The Messenger*, 127
- Gómez-Leal, I., Kaltenecker, L., Lucarini, V., & Lunkeit, F. 2018, *The Astrophysical Journal*, 869, 129, doi: [10.3847/1538-4357/aaea5f](https://doi.org/10.3847/1538-4357/aaea5f)
- Gómez-Leal, I., Kaltenecker, L., Lucarini, V., & Lunkeit, F. 2019, *Icarus*, 321, 608, doi: <https://doi.org/10.1016/j.icarus.2018.11.019>
- Green, A. E. S. 1964, *Appl. Opt.*, 3, doi: [10.1364/AO.3.000203](https://doi.org/10.1364/AO.3.000203)
- Greene, T. P., Line, M. R., Montero, C., et al. 2016, *ApJ*, 817, 17, doi: [10.3847/0004-637X/817/1/17](https://doi.org/10.3847/0004-637X/817/1/17)

- Grieger, B., Segschneider, J., Keller, H., et al. 2004, *Advances in Space Research*, 34, 1650 , doi: <https://doi.org/10.1016/j.asr.2003.08.079>
- Heng, K., & Vogt, S. S. 2011, ArXiv e-print
- Hoskins, B. J., & Simmons, A. J. 1975, *Quarterly Journal of the Royal Meteorological Society*, 101, 637, doi: [10.1002/qj.49710142918](https://doi.org/10.1002/qj.49710142918)
- Hourdin, F., Musat, I., Bony, S., et al. 2006, *Climate Dynamics*, 27, 787, doi: [10.1007/s00382-006-0158-0](https://doi.org/10.1007/s00382-006-0158-0)
- Howard, W. S., Tilley, M. A., Corbett, H., et al. 2018, *The Astrophysical Journal Letters*, 860, L30. <http://stacks.iop.org/2041-8205/860/i=2/a=L30>
- Hu, Y., Vaughan, M., McClain, C., et al. 2007, *Atmospheric Chemistry and Physics*, 7, 3353, doi: [10.5194/acp-7-3353-2007](https://doi.org/10.5194/acp-7-3353-2007)
- Jenkins, J. S., Harrington, J., Challener, R. C., et al. 2019, *MNRAS*, 487, 268, doi: [10.1093/mnras/stz1268](https://doi.org/10.1093/mnras/stz1268)
- Joshi, M. M., & Haberle, R. M. 2012, *Astrobiology*, 12, 3, doi: [10.1089/ast.2011.0668](https://doi.org/10.1089/ast.2011.0668)
- Joshi, M. M., Haberle, R. M., & Reynolds, R. T. 1997, *Icarus*, 129, doi: <https://doi.org/10.1006/icar.1997.5793>
- Kane, S. R., & Gelino, D. M. 2012, *PASP*, 124, 323, doi: [10.1086/665271](https://doi.org/10.1086/665271)
- Kane, S. R., Gelino, D. M., & Turnbull, M. C. 2017, *AJ*, 153, 52, doi: [10.3847/1538-3881/153/2/52](https://doi.org/10.3847/1538-3881/153/2/52)
- Kasting, J. F., Whitmire, D. P., & Reynolds, R. T. 1993, *Icarus*, 101, doi: <https://doi.org/10.1006/icar.1993.1010>
- Kelsall, T., Weiland, J. L., Franz, B. A., et al. 1998, *ApJ*, 508, 44, doi: [10.1086/306380](https://doi.org/10.1086/306380)
- Kendrew, S., Jolissaint, L., Brandl, B., et al. 2010, *Society of Photo-Optical Instrumentation Engineers (SPIE) Conference Series*, Vol. 7735, Mid-infrared astronomy with the E-ELT: performance of METIS (SPIE), 77355F, doi: [10.1117/12.857043](https://doi.org/10.1117/12.857043)
- Kervella, P., Arenou, F., & Schneider, J. 2020, *A&A*, 635, L14, doi: [10.1051/0004-6361/202037551](https://doi.org/10.1051/0004-6361/202037551)
- Kipping, D. M., Cameron, C., Hartman, J. D., et al. 2017, *AJ*, 153, 93, doi: [10.3847/1538-3881/153/3/93](https://doi.org/10.3847/1538-3881/153/3/93)
- Knietzsch, M.-A., Schröder, A., Lucarini, V., & Lunkeit, F. 2015, *Earth System Dynamics*, 6, 591, doi: [10.5194/esd-6-591-2015](https://doi.org/10.5194/esd-6-591-2015)
- Komacek, T. D., & Abbot, D. S. 2019, *ApJ*, 871, 245, doi: [10.3847/1538-4357/aafb33](https://doi.org/10.3847/1538-4357/aafb33)
- Kopp, G. 2018, in *Comprehensive Remote Sensing*, ed. S. Liang (Oxford: Elsevier), 32 – 66, doi: <https://doi.org/10.1016/B978-0-12-409548-9.10366-5>
- Kreidberg, L., & Loeb, A. 2016, *The Astrophysical Journal Letters*, 832, L12. <http://stacks.iop.org/2041-8205/832/i=1/a=L12>
- Krick, J. E., Glaccum, W. J., Carey, S. J., et al. 2012, *ApJ*, 754, 53, doi: [10.1088/0004-637X/754/1/53](https://doi.org/10.1088/0004-637X/754/1/53)
- Kuhn, J. R., Berdyugina, S. V., Capsal, J.-F., et al. 2018, in *Society of Photo-Optical Instrumentation Engineers (SPIE) Conference Series*, Vol. 10700, Ground-based and Airborne Telescopes VII, 1070015, doi: [10.1117/12.2312779](https://doi.org/10.1117/12.2312779)
- Kunz, T., Fraedrich, K., & Lunkeit, F. 2009, *Journal of the Atmospheric Sciences*, 66, 2288, doi: [10.1175/2009JAS2827.1](https://doi.org/10.1175/2009JAS2827.1)
- Linsenmeier, M., Pascale, S., & Lucarini, V. 2015, *Planetary and Space Science*, 105, 43 , doi: <https://doi.org/10.1016/j.pss.2014.11.003>
- Liu, H.-G., Jiang, P., Huang, X., et al. 2018, *AJ*, 155, 12, doi: [10.3847/1538-3881/aa9b86](https://doi.org/10.3847/1538-3881/aa9b86)
- Lovis, C., Snellen, I., Mouillet, D., et al. 2017, *A&A*, 599, A16, doi: [10.1051/0004-6361/201629682](https://doi.org/10.1051/0004-6361/201629682)
- Lovric, M., Tosone, F., Pietropaolo, E., et al. 2017, *J. Space Weather Space Clim.*, 7, A6, doi: [10.1051/swsc/2017001](https://doi.org/10.1051/swsc/2017001)
- Loyd, R. O. P., France, K., Youngblood, A., et al. 2016, *The Astrophysical Journal*, 824, doi: [10.3847/0004-637X/824/2/102](https://doi.org/10.3847/0004-637X/824/2/102)
- Lucarini, V., Fraedrich, K., & Lunkeit, F. 2010a, *Atmospheric Chemistry and Physics*, 10, 9729, doi: [10.5194/acp-10-9729-2010](https://doi.org/10.5194/acp-10-9729-2010)
- . 2010b, *Quarterly Journal of the Royal Meteorological Society*, 136, 2, doi: [10.1002/qj.543](https://doi.org/10.1002/qj.543)
- Lucarini, V., Pascale, S., Boschi, R., Kirk, E., & Iro, N. 2013, *Astronomische Nachrichten*, 334, 576, doi: [10.1002/asna.201311903](https://doi.org/10.1002/asna.201311903)
- Lunkeit, F., Fraedrich, K., & Bauer, S. E. 1998, *Climate Dynamics*, 14, 813, doi: [10.1007/s003820050257](https://doi.org/10.1007/s003820050257)
- Madronich, S. 1987, *Journal of Geophysical Research Atmospheres*, 92(D8), 9750, doi: [10.1029/JD092iD08p09740](https://doi.org/10.1029/JD092iD08p09740)
- Manabe, S., & Möller, F. 1961, *Monthly Weather Review*, 89, doi: [10.1175/1520-0493\(1961\)089<0503:OTREAH>2.0.CO;2](https://doi.org/10.1175/1520-0493(1961)089<0503:OTREAH>2.0.CO;2)
- Maurin, A. S., Selsis, F., Hersant, F., & Belu, A. 2012, *A&A*, 538, A95, doi: [10.1051/0004-6361/201117054](https://doi.org/10.1051/0004-6361/201117054)
- Meadows, V. S., Arney, G. N., Schwieterman, E. W., et al. 2018, *Astrobiology*, 18, 133, doi: [10.1089/ast.2016.1589](https://doi.org/10.1089/ast.2016.1589)
- Merlis, T. M., Schneider, T., Bordoni, S., & Eisenman, I. 2013, *Journal of Climate*, 26, doi: [10.1175/JCLI-D-12-00149.1](https://doi.org/10.1175/JCLI-D-12-00149.1)
- Pascale, S., Ragone, F., Lucarini, V., Wang, Y., & Boschi, R. 2013, *Planetary and Space Science*, 84, 48 , doi: <https://doi.org/10.1016/j.pss.2013.04.014>
- Pérez-Muñuzuri, V., Deza, R., Fraedrich, K., Kunz, T., & Lunkeit, F. 2005, *Physical review. E, Statistical, nonlinear, and soft matter physics*, 71 6 Pt 2, 065602

- Petty, G. W. 2006, *A first course in atmospheric radiation* (Sundog Publishing, Madison, Wisconsin)
- Reach, W. T., Franz, B. A., & Weiland, J. L. 1997, *Icarus*, 127, 461, doi: [10.1006/icar.1997.5704](https://doi.org/10.1006/icar.1997.5704)
- Ribas, I., Gregg, M. D., Boyajian, T. S., & Bolmont, E. 2017, *A&A*, 603, A58, doi: [10.1051/0004-6361/201730582](https://doi.org/10.1051/0004-6361/201730582)
- Ribas, I., Bolmont, E., Selsis, F., et al. 2016, *Astronomy and Astrophysics*, 596, doi: [10.1051/0004-6361/201629576](https://doi.org/10.1051/0004-6361/201629576)
- Romanova, V., Lohmann, G., & Grosfeld, K. 2006, *Climate of the Past*, 2., 31. www.clim-past.net/2/31/2006/
- Sasamori, T. 1968, *Journal of Applied Meteorology*, 7, 721, doi: [10.1175/1520-0450\(1968\)007\(0721:TRCCFA\)2.0.CO;2](https://doi.org/10.1175/1520-0450(1968)007(0721:TRCCFA)2.0.CO;2)
- Schmittner, A., Silva, T. A. M., Fraedrich, K., Kirk, E., & Lunkeit, F. 2011, *Journal of Climate*, 24, 2814, doi: [10.1175/2010JCLI3982.1](https://doi.org/10.1175/2010JCLI3982.1)
- See, V., Jardine, M., Vidotto, A. A., et al. 2014, *A&A*, 570, A99, doi: [10.1051/0004-6361/201424323](https://doi.org/10.1051/0004-6361/201424323)
- Segschneider, J., Grieger, B., Keller, H., et al. 2005, *Planetary and Space Science*, 53, 659, doi: <https://doi.org/10.1016/j.pss.2004.10.003>
- Seiffert, R., Blender, R., & Fraedrich, K. 2007, *Quarterly Journal of the Royal Meteorological Society*, 132, 1627, doi: [10.1256/qj.05.139](https://doi.org/10.1256/qj.05.139)
- Selsis, F., Wordsworth, R. D., & Forget, F. 2011, *A&A*, 532, A1, doi: [10.1051/0004-6361/201116654](https://doi.org/10.1051/0004-6361/201116654)
- Shields, A. L., Meadows, V. S., Bitz, C. M., et al. 2013, *Astrobiology*, 13, 715, doi: [10.1089/ast.2012.0961](https://doi.org/10.1089/ast.2012.0961)
- Showman, A. P., & Guillot, T. 2002, *Astronomy and Astrophysics*, 385, doi: [10.1051/0004-6361:20020101](https://doi.org/10.1051/0004-6361:20020101)
- Showman, A. P., & Polvani, L. M. 2011, *The Astrophysical Journal*, 738
- Showman, A. P., Wordsworth, R. D., Merlis, T. M., & Kaspi, Y. 2013, *Comparative Climatology of Terrestrial Planets*
- Stamnes, K., Tsay, S.-C., Wiscombe, W., & Jayaweera, K. 1988, *Appl. Opt.*, 27, 2502, doi: [10.1364/AO.27.002502](https://doi.org/10.1364/AO.27.002502)
- Stenzel, O., Grieger, B., Keller, H., et al. 2007, *Planetary and Space Science*, 55, 2087, doi: <https://doi.org/10.1016/j.pss.2007.09.001>
- Suárez Mascareño, A., Faria, J. P., Figueira, P., et al. 2020, *A&A*, 639, A77, doi: [10.1051/0004-6361/202037745](https://doi.org/10.1051/0004-6361/202037745)
- Swift, D. C., Eggert, J. H., Hicks, D. G., et al. 2012, *ApJ*, 744, 59, doi: [10.1088/0004-637X/744/1/59](https://doi.org/10.1088/0004-637X/744/1/59)
- Tian, F., & Ida, S. 2015, *Nature Geoscience*, 8, 177, doi: [10.1038/ngeo2372](https://doi.org/10.1038/ngeo2372)
- Tsay, S.-C., Stamnes, K., Wiscombe, W., Laszlo, I., & Einaudi, F. 2000, *General Purpose Fortran Program for Discrete-Ordinate-Method Radiative Transfer in Scattering and Emitting Layered Media: An Update of DISORT*, Tech. rep., NASA Goddard Space Flight Center
- Turbet, M., Leconte, J., Selsis, F., et al. 2016, *Astronomy and Astrophysics*, 596, doi: [10.1051/0004-6361/201629577](https://doi.org/10.1051/0004-6361/201629577)
- van der Blik, N. S., Manfroid, J., & Bouchet, P. 1996, *Astron. Astrophys. Suppl. Ser.*, 119, doi: [10.1051/aas:1996267](https://doi.org/10.1051/aas:1996267)
- Walters, D., Baran, A., Boutle, I., et al. 2017, *Geoscientific Model Development Discussions*, 2017, 1, doi: [10.5194/gmd-2017-291](https://doi.org/10.5194/gmd-2017-291)
- Wells, M., Pel, J.-W., Glasse, A., et al. 2015, *Publications of the Astronomical Society of the Pacific*, 127
- Wordsworth, R. D., Forget, F., Selsis, F., et al. 2011, *The Astrophysical Journal Letters*, 733
- Yang, J., Cowan, N. B., & Abbot, D. S. 2013, *The Astrophysical Journal Letters*, 771. <http://stacks.iop.org/2041-8205/771/i=2/a=L45>
- Youngblood, A., France, K., Loyd, R. O. P., et al. 2016, *The Astrophysical Journal*, 824, doi: [10.3847/0004-637X/824/2/101](https://doi.org/10.3847/0004-637X/824/2/101)
- Zuluaga, J. I., Bustamante, S., Cuartas, P. A., & Hoyos, J. H. 2013, *The Astrophysical Journal*, 770, 23